Growth of surface wind-waves in water of finite depth: A laboratory experiment

H. Branger, M.A. Manna, C. Luneau, M. Abid, C. Kharif

Growth of surface wind-waves in water of finite depth: a laboratory experiment

H. Branger[a,*], M. A. Manna[b], C. Luneau[c], M. Abid[d,a], C. Kharif[d,a]

[a] *Institut de Recherche sur les Phénomènes Hors Équilibre, CNRS, AMU, UMR 7342, 49 rue Frédéric Joliot-Curie, BP 146, 13384 Marseille cedex 13, France.*
[b] *Laboratoire Charles Coulomb, UMR 5221 CNRS-Université de Montpellier, Montpellier, France.*
[c] *OSU-Pytheas, CNRS, Aix-Marseille Université, Marseille, France.*
[d] *Ecole Centrale Marseille, 38 rue Frédéric Joliot-Curie, 13451 Marseille cedex 20, France.*

Abstract

This paper reports on laboratory experiment results on wind-driven surface waves in finite depth and their comparison with theoretical predictions and experimental in-situ studies. We introduce the Miles theory's extension to the case of finite depth, as well as the rules transforming theoretical expressions to formulae commonly used in experimental routines, in particular the important rules transforming theoretical growth rates to experimental ones. Wind waves depend strongly on boundary marine layer parameters, namely, the aerodynamic roughness length, the Charnock constant, as well as the drag coefficient. Consequently, this work gives detailed measurements of these parameters in finite depths. Experiments conducted in the IRPHÉ/Pythéas wind-wave tank (Marseille, France), reveal that for a given wind speed, these values are higher in finite depth than in deep water. In the limit case of fully developed surface, due to depth, theoretical and empirical formulas relating the critical values of wave age to the non-dimensional depth have been experimentally verified. Plots of non-dimensional peak frequency, non-dimensional energy, and the inverse of wave age, against non-dimensional depth are presented. The plots clearly show that these quantities admit a limit due to the depth influence. All data obey the range of empirical values established in field experiments. Experimental data, obtained in the facility, agree with the theoretical family of depth-dependent wave growth rate as a function of wave age in finite depth. The non-dimensional growth-rate data obtained in our laboratory, as a function of the inverse of wave age, are consistent with the theoretical predictions of Miles theory in finite depth ([Montalvo et al., 2013 a,b; Latifi et al., 2017], as well as measurements from other laboratories.

Keywords: Wind-generated waves; wind-wave growth rates; Miles' theory; finite depth; wind-wave facility;

*Main corresponding author
Email address: branger@irphe.univ-mrs.fr (H. Branger)

1. Introduction

Understanding the coupling between the atmosphere and the ocean surface is important for many scientific, environmental and engineering problems. The wind driven momentum exchange and amplification factor of the water waves by the wind at the air-water interface are key drivers of hydrodynamic and ecological processes in open seas. Surface water waves and their generation by wind is a fascinating issue. The task of coupling atmosphere and oceans requires rather detailed knowledge of the wave-field and, in particular, the momentum transfer between boundary layer winds and surface waves. While coastal zones are limited, compared to the global ocean, their impacts on and response to human activity are profound and should be better understood. The vast majority of air-sea interaction studies involved measurements made across the open ocean and, excepting relatively few studies, the role transition in the momentum flux from open ocean to nearshore has not been fully characterized: amplification of water waves by the wind in finite depth environment is still an unsolved problem. Despite differentiated observed physical air-sea behaviours between deep waters and shallow waters, atmospheric models apply the same wind stress formulation regardless of the depth of the waters. Wave growth parametrizations for deep water are commonly applied to shallow water, although the impact that depth-limited processes have on the growtfh of the waves by the wind remains under-explored. Additional well-controlled experiments are essential to gain a better understanding of the growth of waves over water of finite depth. Any theory needs ultimate validation by experimental means.

A few experiments have been conducted to study the influence of the water depth on air-sea interactions at the water surface. Most of them were dedicated to the role of the finite depth h on the modification of prediction laws of non-dimensional energy ($g^2\sigma^2/U_{ref}^4$), non-dimensional frequency (fU_{ref}/g), wave age (c/U_{ref}), non-dimensional fetch (gX/U_{ref}^2) and non-dimensional depth (gh/U_{ref}), with σ the standard deviation of the water elevation, U_{ref} the wind speed at a reference level, g the acceleration due to gravity, f the dominant wave frequency, c the wave celerity and X the fetch [Thijsse, 1949; Bretschneider, 1954, 1958; Ijima and Tang, 1966; CERC, 1977, 1984; Young and Verhagen, 1996 a,b].

Other studies were done on the influence of water depth on momentum flux ($\tau = \rho_a u*^2$), with ρ_a the air density, $u*$ the friction velocity [Geernaert, 1987; Donelan et al., 2005, 2006; Zhao et al., 2015; Ortiz-Suslow et al., 2018; Chen et al., 2019], on the drag coefficient ($C_d = u*^2/U_{ref}^2$) [Anctil and Donelan, 1986; Donelan et al., 2012; Bi et al., 2015; Oost et al., 2002; Toffoli et al., 2012; Shabani et al., 2014], or on the roughness length z_0 [Anctil and Donelan, 1986; Smith, 1980; Gao et al., 2009; MacMahan, 2017; Jimenez and Dudhia, 2018]. These papers show the increase of both $u*$, C_d and z_0 in shallow water environment. Authors explain this increase by the modification of wave dynamics and kinematics by the shallow bottom. Finite depth decreases the wave celerity c, thus the wave age c/U_{ref}, and increases wave height and wave steepness by shoaling effect. This modification of celerity and wave geometric profile seems to explain the increase of drag and roughness. Very close to the shore, the slower wave celerity and the sawtooth wave shape in the surf zone are an important contributor to the increased wind stress. For example, [Donelan et al., 2006] argued that shallow water measurements exhibit higher drag coefficients for same wind speed, because the waves of the same frequency are slower and shorter and consequently steeper, thus producing higher stress. Based on their air-flow separation model, [Makin and Kudryavtsev, 2002] have reproduced the increase in C_d with decreasing water depth: at moderate and high winds, decreasing water depth induces a steepening of dominant waves and thus more air-flow separation at the crest of the waves, and then more drag. The constant flux model of [Chen et al., 2019] has shown how the waves, modified by the bottom in finite depth conditions, influence the wind profile over the waves and thus the stress budget between the water and the air. Other writers like MacMahan [2017] related the increase of roughness near the coasts to surf-zone foam coverage due to wave breaking. Recently [Ortiz-Suslow et al., 2018] clearly demonstrated that the mechanisms that characterize air-sea interaction in deep water may not apply near shore in finite depth waters.

Very few papers [Young and Verhagen, 1996 a,b; Donelan et al., 2005, 2006; Young, 1997; Young et al., 2005] were dedicated specifically to the growth rate modification by the water depth. The experi-

ment described in [Young and Verhagen, 1996 a] was the first really comprehensive attempt to measure the evolution of fetch limited waves in water of finite depth. The Lake George finite-depth field experiment is well-documented in literature and we refer to [Young et al., 2005] for the most complete and detailed summary on this experiment. A large set of atmospheric and wave data were collected in finite water depth regimes at the Lake George measurement site. The aim of the Lake George project was to simultaneously measure source and sink functions for wave prediction models, as well as fetch-limited wave evolution. In particular, the effects of water depth and wave steepness were addressed. The lake George measurements have confirmed the water depth dependence of the asymptotic limits to wave growth. Young [1997], also reproduced in Young [1999], derived an empirical relation with appropriate non-dimensional parameters able to reproduce the experimental data of Young and Verhagen [1996 a]. In particular the relationship between the variation of fractional energy and the inverse wage age, found by Donelan et al. [1992] for deep water, was extended to the finite depth domain. These open field results together with plots of the empirical laws have shown that, contrary to the deep water case, the wave age at which the growth rate becomes zero is wind-dependent and depth-dependent. In Young [1997] the curves of the wave growth versus wave age have been presented for ranges of a non-dimensional water depth parameter δ. Beyond a critical wave age, the growth rate vanishes.

Pioneering theories on surface wind-wave growth have been developed for deep water waves since [Jeffreys, 1924, 1925; Phillips, 1957] and [Miles, 1957], and until more recently, for example by [Belcher and Hunt, 1993] or other authors reviewed in [Janssen, 2004]. These theories are thus restrictive with regard to wind generated near-shore waves, bays, rivers or shallow lake waves. The well known Miles' theory has been extended to the finite depth under breeze to moderate wind conditions by several authors [Montalvo et al., 2013 a,b; Latifi et al., 2017]. They derived a surface wind-wave growth theory in finite depth based on a) the Euler equations in the water domain for finite depth, and b) the linearised governing equation of steady air flow, with a prescribed mean horizontal velocity U(z) depending on the vertical coordinate z together with perturbations to the mean. Developments lead to the well known Rayleigh equation [Rayleigh, 1880]. Then a non-dimensional water depth parameter depending on the depth and on a characteristic wind speed, induced a family of curves representing the wave growth as a function of the wave phase velocity and the wind speed. Their model provides an agreement with the data and empirical relationships obtained from the Lake George experiment and the Australian Shallow Water Experiment. For small wave age the wave growth rates are comparable to those of deep water, but for higher wave age a finite-depth limited growth is reached, with wave growth rates going to zero. The [Montalvo et al., 2013 a] study was focused on the wave growth of monochromatic waves, the work of [Montalvo et al., 2013 b] was extended to the evolution of wave packets growing with the wind, and [Latifi et al., 2017] added the effect of shelter mechanism in the theory [Jeffreys, 1925], and they also added non-linearity effects and studied the evolution of non-linear breathers and solitons in shallow depth environments and windy conditions.

To date, there is no referenced laboratory direct experimental work that confirms or denies the theoretical study of [Montalvo et al., 2013 a,b; Latifi et al., 2017], more particularly the fact that the wave growth rate induced by the wind could drop to zero amplification for some configurations of water depth, wave dominant frequency, wave age and wind speed. Recently amazing new laboratory experiments have been conducted on air-to-water transfers using laser doppler Anemometry (LDA) or particle Image Velocimetry (PIV) to characterize wave amplification by the wind through form drag and viscous drag repartition along the water surface [Veron et al., 2007; Buckley et al., 2020; Yousefi K. and M.P, 2021b,a; Kozlova and Troitskaya, 2021; Kabardin et al., 2020]. Unfortunately, all these experimental works with optical methods have always been conducted on deep-water conditions and not in intermediate or shallow water conditions. Moreover, they were often done in moderate to high wind speed conditions because most of the studies were focused on airflow separation and aerosol production.

Therefore a well-control experiment on wave growth in finite depth environment is lacking. The goal of our study is to conduct a specific water tank experiment with wind blowing over the water surface, and with different combinations of water depth, dominant waves, and wind speeds. Marine air

boundary layer characteristics (friction velocities, drag coefficients, surface roughness lengths) will be estimated, and water elevation will be measured at different locations to measure the wave growth in relatively smooth wind and low steepness conditions: we avoided wave breaking dissipation, because in [Montalvo et al., 2013 a,b; Latifi et al., 2017] theories breaking dissipation is disregarded. Wave growth will be compared to theoretical developments. The asymptotic depth limited growth of non-dimensional energy, non-dimensional peak frequency and inverse wave age will be tested and validated.

Notations, parameters and theoretical developments are presented in section 2. Material and methods are described in section 3, with the presentation of the wind-wave facility, the experimental arrangement, data processing, experimental conditions, air and water measured values and their precision. Section 4 describes the effects of water depth on air flow, on air-water transfer parameters, on wave growth rate, and this section ends by the comparison with theory developments. The last section provides a short summary and outlook.

2. The air-water interface in finite depth. Theoretical wave growth rates γ and β

2.1. Wave growth rates γ and β : analytical developments

The classical Miles' theory in deep water is based on the dispersion relation of the air-sea interface and the related Rayleigh equation [Rayleigh, 1880; Conte and Miles, 1959; Drazin and Reid, 1982]. We consider the water and air particles to be located relative to a two-dimensional Cartesian coordinate system with axes x, z, origin $x = z = 0$, $x \in [-\infty, +\infty]$, z being the upward vertical direction and $z \in [-h, +\infty]$. Before perturbations the water lies between the impermeable bottom à $z = -h$ and the still water surface at $z = 0$. The undisturbed water steady state is incompressible, inviscid and with zero surface tension. It is assumed that the air is also inviscid and incompressible. In absence of surface waves the air can be described by a prescribed mean shear flow $U(z)$ in the x-direction which varies with the height z above the surface i.e.:

$$\vec{U} = U(z)\vec{e}_x \tag{1}$$

with $\vec{e}_x$ the unitary vector in the x direction.
Let us consider a perturbation to the free surface which propagates, under the wind action, like a progressive plane wave of wave number k, phase velocity c and constant amplitude η_0, i.e., $\eta(x,t) = \eta_0 e^{ik(x-ct)}$. Miles's mechanism of wave generation by wind assumes that $\eta(x,t)$ induces small perturbations of the air pressure and velocities. From reference [Montalvo et al., 2013 a] we have that the perturbed air pressure $P_a(x,z,t)$ is given by

$$P_a(x,z,t) = P_0 - \rho_a g z + ik\rho_a \int_z^\infty [U(z) - c] w_a(x,z,t) dz \tag{2}$$

where P_0 is the atmospheric pressure, ρ_a the air density, $w_a(x,z,t) = \mathcal{W}_a(z)e^{ik(x-ct)}$ the z-component of the perturbed air velocity. The expression for P_a is of primary importance in the Miles mechanism of wave-generation by wind since it is supposed that the momentum transfer from the air into the surface waves is due to the air pressure oscillations in quadrature with the surface slope [Deardorff, 1967].

In (2) neither $w_a(x,z,t)$ nor c are known. The perturbed velocity $w_a(x,z,t)$ is calculated using the Rayleigh equation [Montalvo et al., 2013 a] and c is determined by the relation dispersion which reads

$$\rho_w \, \eta(x,t) \, (c^2 k \coth kh - g) + P_0 = P_a(x,\eta,t). \tag{3}$$

In the single-domain problem $P_a(x,\eta,t) = P_0$ and equation (3) brings to the usual expression c_0 of the phase velocity governing surface waves in finite depth: $c = c_0 = \sqrt{(g/k)\tanh(kh)}$. In this case in order to calculate c from (3) we use P_a evaluated at $z = \eta$ from (2). We obtain [Montalvo et al., 2013 a]

$$g(1-s) + c\frac{sk^2}{W_0} I_1 - c^2\left(\frac{sk^2}{W_0} I_2 + k\coth(kh)\right) = 0, \tag{4}$$

with

$$I_1 = \int_{z_0}^{\infty} U(z)\mathcal{W}_a(z)dz, \quad I_2 = \int_{z_0}^{\infty} \mathcal{W}_a(z)dz, \tag{5}$$

with z_0 the aerodynamic sea surface roughness located just above the interface, $W_0 = \lim_{z\to z_0} \mathcal{W}_a(z)$, and s the ratio of air density to water density: $s = (\rho_a/\rho_w) \sim 10^{-3}$.

The function $\mathcal{W}_a(z)$ is complex and consequently c too, so $c = \mathrm{Re}\{(c)\} + i\,\mathrm{Im}\{(c)\}$ where $\mathrm{Im}\{(c)\}$ ($\mathrm{Re}\{(c)\}$) is the imaginary (real) part of c. The parameter s is small ($\rho_a/\rho_w \sim 10^{-3}$) and the solution of (4) may be approximated as

$$c = c_0 + sc_1 + O(s^2). \tag{6}$$

c_0 is real, so the imaginary part $\mathrm{Im}\{(c)\}$ is $s\,\mathrm{Im}\{(c_1)\}$, and it gives the growth rate of $\eta(x,t)$ defined by

$$\gamma = k\,\mathrm{Im}\{(c)\} = sk\,\mathrm{Im}\{(c_1)\} \tag{7}$$

The theoretical and numerical results concerning the growth rate γ are studied and computed with three non-dimensional parameters δ, θ_{dw} and θ_{fd} defined by

$$\delta = \frac{gh}{U_1^2}, \quad \theta_{dw} = \frac{1}{U_1}\sqrt{\frac{g}{k}}, \quad \theta_{fd} = \theta_{dw}\sqrt{T_{kh}}, \quad \text{with,} \quad T_{kh} = \tanh(kh) = \tanh\left(\frac{\delta}{\theta_{dw}^2}\right) \tag{8}$$

The non-dimensional parameter δ, for constant U_1, measures the influence of the finite fluid depth on the rate of growth of $\eta(x,t)$. The parameter θ_{dw} is a *theoretical analogous of the deep water wave age*. It measures the relative value of the deep water phase speed in relation to the characteristic wind velocity U_1. Finally θ_{fd} is *a finite depth wave age* θ_{fd}. We introduce the following non-dimensional variables and scaling, hats meaning non-dimensional quantities

$$U = U_1\hat{U}, \quad \mathcal{W}_a = W_0\hat{\mathcal{W}}_a, \quad z = \frac{\hat{z}}{k}, \quad c = U_1\hat{c}, \quad t = \frac{U_1}{g}\hat{t}. \tag{9}$$

Using (6) and (9) in equation (4) and retaining only the terms of order $\mathcal{O}(s)$ we obtain $\hat{c}$,

$$\hat{c} = \hat{c_0} + s\hat{c}_1 = \theta_{dw}T_{kh}^{1/2} - \frac{s}{2}\theta_{dw}T_{kh}^{1/2} + \frac{s}{2}\{T_{kh}\hat{I}_1 - \theta_{dw}T_{kh}^{3/2}\hat{I}_2\}, \tag{10}$$

and with (7), (9) and (10 , we derive the non-dimensional growth rate $\hat{\gamma} = \frac{U_1}{g}\gamma$ which reads

$$\hat{\gamma} = \frac{s}{2}\left(\frac{T_{kh}\,\mathrm{Im}\left\{\hat{I}_1\right\}}{\theta_{dw}^2} - \frac{T_{kh}^{3/2}\,\mathrm{Im}\left\{\hat{I}_2\right\}}{\theta_{dw}}\right). \tag{11}$$

From the coupled water/air interface, [Miles, 1957] derived the phase velocity as :

$$c^2 = c_0^2 + \frac{\rho_a}{\rho_w}(\alpha + i\beta)^2U_1^2 \tag{12}$$

where α and β are non-dimensional coefficients. Using (6) we obtain

$$\alpha = \frac{2c_0\,\mathrm{Re}\{(c_1)\}}{U_1^2}, \quad \text{and} \quad \beta = \frac{2c_0\,\mathrm{Im}\{(c_1)\}}{U_1^2} \tag{13}$$

where β is the β-*Miles* parameter. Using $\hat{\gamma} = \frac{U_1}{g}\gamma$, and equations (8) and (9), we obtain the following transformation rule between non-dimensional parameters β and $\hat{\gamma}$

$$\beta = \frac{2\hat{\gamma}}{s}\theta_{dw}^3T_{kh}^{1/2}, \tag{14}$$

The deep water limit $\delta \to \infty$ ($T_{kh} \to 1$) gives back $\hat{\gamma}$ and β for Miles' theory. The existence of a finite depth h transforms the unique curve of wave growth rate $\hat{\gamma}$ or β in deep water in a *family of curves* indexed by $\delta = gh/U_1^2$, i.e., a curve for each value of δ [Montalvo et al., 2013 a,b; Latifi et al., 2017].

2.2. Wave growth rates γ and β : wind-wave tank environment

Experimental results are obtained using appropriate parameters and formulae commonly employed in the laboratory routine. In this section we are looking for the transformation rules between theoretical expressions and their laboratory counterpart.

Let us consider a monochromatic progressive wave moving in a wave tank. The wave frequency is ω, the wavenumber k and the amplitude $a(x,t)$ with x the distance from the wavemaker which is termed the *fetch* x and t is the time

$$\eta(x,t) = a(x,t)\sin(kx - \omega t) \tag{15}$$

If we consider the wind action, with wind U_{ref} (the wind speed at the altitude $z = z_{ref}$), as the unique process causing the wave growth, and we consider the viscosity and bottom friction the only two existing mechanisms of wave dissipation, (i.e. no wave breaking because we did not see wave breaking during our experiments, and the present theory excludes wave breaking), we may write :

$$(\frac{1}{a}\frac{\partial a}{\partial x})_{|U_{ref}} = \gamma_{es} - \nu \tag{16}$$

where γ_{es} *is the experimental spatial wave growth rate* , and ν is the total rate of dissipation by viscosity and friction along the walls and on the bottom of the tank.

For each experiment we did two runs: the first one was done with mono-frequency paddle waves with amplitude a, frequency ω and wind speed U_{ref} and the second one was done with the same mono-frequency waves (amplitude a, and frequency ω) but without wind speed, *i.e.* with $U_{ref} = 0$ m/s. When there is no wind speed, the wind notation is U_0.

We made the strong hypothesis that the dissipation process was the same in presence of wind and without wind. This hypothesis is questionable because there may have many efficient processes that dissipate the waves in a closed basin [Miles, 1967]. Molecular viscosity and friction dissipation along the bottom and along the tank walls are always an active process and occur in all conditions [Van Dorn, 1966]. Wave breaking is another strong dissipation process but it occurs with steep waves and/or during moderate to strong wind conditions, and/or very close to the shore-line [Perlin et al., 2013]. Droplets and spume generation is also an efficient dissipation process, but it occurs only at relatively high winds Veron [2015]. Another process could be the non-linear interaction between the shear-water current generated by the wind drag at the surface, and the orbital velocities of the waves leading to possible wave attenuation. But this phenomenon of interaction between water vorticity and water waves is not well-known and quite impossible to quantify Hsu et al. [2018]. We decided to avoid it. Air-flow separation, occurring at the crest of steep, breaking or near breaking waves, generates vortical motions in the air that may contribute to the dissipation of wave energy Iafrati et al. [2014]. But we were always in low steep waves environment, and we did not take this effect into account. In our study, we always generate low steep mechanical paddle waves and conducted runs with low wind speed in order to avoid wave breaking, aerosol production, and air-flow separation above waves. This is the reason why we made the strong hypothesis that the main dissipation process was the molecular viscosity.

So without wind we may write:

$$(\frac{1}{a}\frac{\partial a}{\partial x})_{|U_0} = -\nu \tag{17}$$

Finally, the spatial growth rate may be inferred from (16) and (17)

$$(\frac{1}{a}\frac{\partial a}{\partial x})_{|U_{ref}} - (\frac{1}{a}\frac{\partial a}{\partial x})_{|U_0} = \gamma_{es} \tag{18}$$

In many papers, model theories and wave prediction models, the temporal growth rate γ [Janssen, 2004; Montalvo et al., 2013 a,b] or the temporal growth rate β_{Miles} [Miles, 1957] are used instead of

the spatial growth rate. By analogy we can define an experimental temporal wave growth rate γ_{et}, related to the experimental spatial growth rate γ_{es} by the group velocity C_g [Gaster, 1962] :

$$\gamma_{et} = C_g \, \gamma_{es} \tag{19}$$

The non-dimensional temporal wave growth $\hat{\gamma}_{et}$ may be defined as [Latifi et al., 2017] :

$$\hat{\gamma}_{et} = (\frac{u*}{g\kappa})\gamma_{et} \tag{20}$$

with $u*$ the friction velocity and $\kappa = 0.41$ the von Karman constant.

[Miles, 1957] used the other non-dimensional temporal wave growth β :

$$\beta = 2\,(\frac{c}{u*})^2\,\kappa^2\frac{1}{\omega}(\frac{1}{\frac{\rho_a}{\rho_w}})\,\gamma_{et} \tag{21}$$

Another widely used non-dimensional temporal growth rate [Plant, 1982; Belcher et al., 1994; Young, 1997] is $\frac{\gamma_{et}}{f} = \frac{\gamma_{et}2\pi}{\omega}$

Experimentally, if the wave height is measured at two different fetches (i.e. different distances from the wind inlet and the wavemaker), namely a_0 and a_1 at fetch x_0 (close to the beginning of the tank) and x_1 (far away from x_0), the dimensional spatial growth rate may be estimated by (c.f. equation (18)):

$$\gamma_{es} = (\frac{1}{a_1}\frac{a_1 - a_0}{x_1 - x_0})_{|U_{ref}} - (\frac{1}{a_1}\frac{a_1 - a_0}{x_1 - x_0})_{|U_0} \tag{22}$$

In this relation, subscripts U_{ref} and U_0 refer to experiments with wind speed U_{ref} and experiments with wind speed $U_0 = 0$

The non-dimensional temporal growth rates $\hat{\gamma}_{et}$, β and $\frac{\gamma_{et}}{f}$ could be estimated by (c.f. equations (19), (20)and (21)):

$$\hat{\gamma}_{et} = (\frac{u*}{g\kappa})\,C_g\,((\frac{1}{a_1}\frac{a_1 - a_0}{x_1 - x_0})_{|U_{ref}} - (\frac{1}{a_1}\frac{a_1 - a_0}{x_1 - x_0})_{|U_0}) \tag{23}$$

$$\beta = 2\,(\frac{c}{u*})^2\,\kappa^2\,\frac{1}{\omega}(\frac{1}{\frac{\rho_a}{\rho_w}})\,C_g\,((\frac{1}{a_1}\frac{a_1 - a_0}{x_1 - x_0})_{|U_{ref}} - (\frac{1}{a_1}\frac{a_1 - a_0}{x_1 - x_0})_{|U_0}) \tag{24}$$

and

$$\gamma_{et}/f = \frac{C_g}{f}\,((\frac{1}{a_1}\frac{a_1 - a_0}{x_1 - x_0})_{|U_{ref}} - (\frac{1}{a_1}\frac{a_1 - a_0}{x_1 - x_0})_{|U_0}) \tag{25}$$

Usually only ω is measured. k is not directly measured. Wavenumber k is estimated by solving the dispersion relationship between k and pulsation w :

$$\omega^2 = gk\,\tanh(kh) \tag{26}$$

In some wave tank experiments, c and C_g are measured using cross-correlation of two or more wave probes located not far from each other [Shemer and Singh, 2021; Longo, 2012]. Unfortunately, during the experiments, the electronic part of the bank of wave gauges usually used in the wind-wave tank was not available and we had only two wave gauges available for the experiments separated by twenty meters. The distance between the two remaining wave gauges was too far to have a good estimation of the wave celerity and wave group by the cross correlation technique. So we decided to use the traditional dispersion relationship to estimate experimentally c and C_g from k :

$$c = c_0 = \sqrt{\frac{g}{k}\,\tanh(kh)} \tag{27}$$

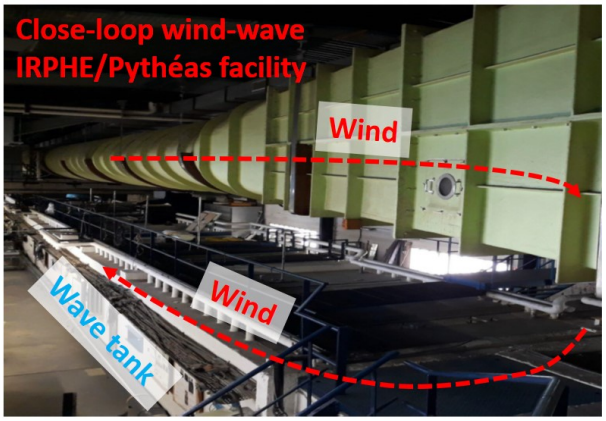

Figure 1: External view of the IRPHÉ/Pythéas wind-wave facility

$$C_g = C_{g0} = \frac{c_0}{2}\,(1 + \frac{2kh}{\sinh(2kh)}) \tag{28}$$

3. Material and methods

3.1. Wind-wave facility and experimental arrangement

Experiments were conducted in the IRPHÉ/Pythéas wind-wave tank, in order to estimate the wave-growth of regular monochromatic mechanical waves under the action of the wind for different water depth configurations. The IRPHÉ/Pythéas wind-wave tank, sketched in Figure 1, consists of a closed-loop tunnel for air-circulation with a 1.5 m-high air cavity above a basin, with a test section 40 m-long and 2.60 m-wide. A complete description of the facility can be found in [Coantic et al., 1981], and at the following address: `https://www.osupytheas.fr/?-Uniqueness-` .The wind is generated by an air blower in the upper part of the tunnel, and guided through a settling chamber with a honeycomb and a converging nozzle. This system produces a uniform airflow at the entrance of the water tank. The bottom is flat, and the water depth may be adjusted from 0.1 m up to 0.80 m depending upon the water quantity put in the tank. An adjustable 6 m-long divergent section was added recently between the entrance of the air section and the water section when the tank is not full of water, thus giving a smooth and non-perturbing air transition between the two air and water sections. The height of this air-divergent can be adjusted to any water depth (see Figure (2)). Consequently for each run, the wind was always tangent to the mean water surface at the entrance of the water section. There is a slightly divergence of the air section along the wind-wave tank, allowing a zero pressure longitudinal gradient, and a constant momentum transfer flux layer from the air to the water along the tank. The air blower is controlled by a graduated potentiometer.

At the upwind-end of the basin, an immersed paddle wave-maker (piston-type) is used for generating monochromatic waves propagating along the wind direction. The wave maker is controlled by a Labview program. These paddle waves do not hit the air divergent located just above them. At the downwind-end, a permeable absorbing beach, with a 6° slope, prevents wave reflection. The reflection rate ranges between 2% to 5% depending upon the wavelength of the incoming waves. The basin side walls are punctuated with windows to observe the water surface. An inside view of the facility showing the experimental arrangement is shown in Figure 3. A sketch of the experimental arrangment is drawn in Figure 4 showing the location of the measuring devices.

The instantaneous horizontal wind velocity was measured with a Constant Temperature Anemometer (E+E Elektronik, Langwiesen, Austria). This sensor was calibrated against a reference sonic GILL

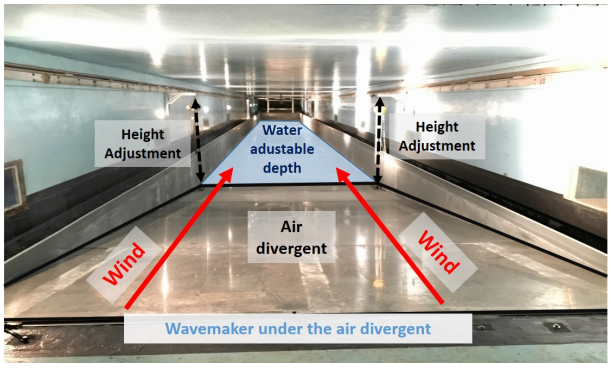

Figure 2: Internal view of the IRPHÉ/Pythéas wind-wave facility: the height of the downwind end of the air-divergent is adjustable, depending upon the water depth. The wavemaker is under the air-divergent. Mechanical waves do not hit the air divergent.

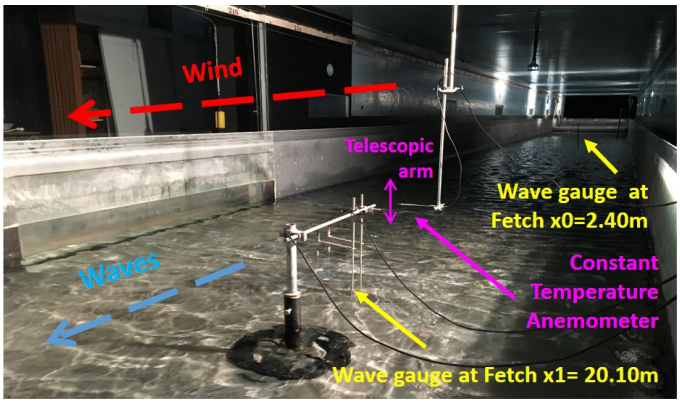

Figure 3: View of the experimental arangment inside the IRPHÉ/Pythéas wind-wave facility. We used one DISA capacitance wave gauge at fetch $x_0 = 2.40$ m, another one at fetch $x_1 = 21.10$ m, a DANTEC Constant Temperature Anemometer (CTA) located on a telescopic arm that can move vertically from the water surface up to 1 m above the waves, thus allowing us to have vertical profiles of horizontal wind speed $U(z)$.

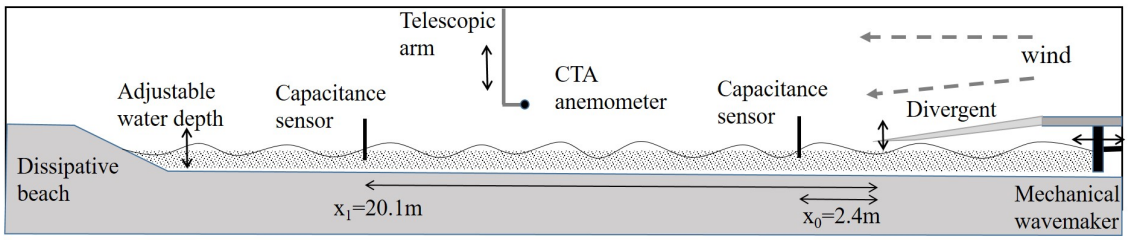

Figure 4: Sketch of the IRPHÉ/Pythéas wind-wave tank facility showing the location of the measuring devices

2D anemometer on several occasions during the experiments.The anemometer was supported by a vertical telescopic pole allowing it to be moved at different heights above the water level. Measurements were done from a point slightly above the highest wave, up to about several vertically distributed points and a duration of 300 s to obtain the vertical profile of the mean horizontal velocity $U(z)$. The precision of the anemometer was about ± 4 cm/s

For these experiments, we used two DISA capacitance-type wave gauges in order to measure the wave growth between two different locations. One wave gauge was located at fetch $x_0 = 2.40$ m, the other one at fetch $x_1 = 20.10$ m. The origin of the fetch ($x = 0$ m), is by definition, the location where the wind hits the water, i.e. at the downwind end of the air divergent. For each run, wave gauges signals were acquired during 20 minutes at a sampling rate of 256 Hz. Before every acquisition, it was verified that the waves in the wave tank were in stationary fetch-limited conditions by waiting a sufficiently long time before acquiring data. Calibrations of the wave gauges were required every day.

3.2. Experimental conditions

Due to: a) the intrinsic mechanical performance of the piston wavemaker in low depth conditions (this wavemaker was designed long time ago for deep waters) , b) the fact that the paddle waves should not hit the rigid air divergent close to the water surface, c) the requirement to have low steep waves to avoid wave amplitude modulation by modulational instabilities and wave breaking, d) the requirement to have low wind speeds to avoid air-flow separation and wave breaking too, the possible combinations of depths, wave frequencies, wave steepnesses, and wind speeds were quite low. We used 4 different water depths, 4 different wave paddle frequencies, and different initial wave amplitudes. Finally we conducted 15 different runs.

Main basic physical parameters characterizing waves and wind are listed in Table 1 . Water depth h ranged from 0.14 m to 0.74 m, mono-frequency waves f_0 from 1.1 Hz to 1.7 Hz, k_0h from 1.07 to 8.59. Finite depth is usually reached when the ratio of water depth over wavelength: h/L_0 is lower than 1/2, which corresponds, in terms of kh to: $kh < \pi = 3.14$. According to the traditional classification of waves with respect to depth [Young, 1999] runs number 1 to 7 and run 10 correspond to intermediate depths: $\pi/10 < kh < \pi$, and other runs to deep water conditions.

Initial steepness $(ak)_0$ ranged from 0.026 to 0.168. Wind speed U_{10} from 3.18 m/s to 5.81 m/s (see next paragraph for the definition and computation of U_{10}). It was not possible to use higher wind speeds and/or higher initial wave steepness because we wanted to avoid natural wave breaking. Wave breaking induces additional wave dissipation which is not included in the theory here. With higher wind speeds or higher initial wave steepnesses we effectively obtained wave breaking inside the wave tank, either by wave amplification by the wind, or by natural sub-harmonic Benjamin-Feir instability leading to strong wave groupiness with the highest wave breaking inside the group [Bliven et al., 1986; Benjamin and Feir, 1967; Hwung et al., 2011].

3.3. Measurements

3.3.1. Wind parameters

In the facility, air and water temperature were roughly at the same temperature, which means that the marine atmospheric conditions were "neutral". The friction velocity $u*$ is considered constant along the test section because of the slightly divergence of the air section along the wind-wave tank allowing a zero pressure longitudinal gradient [Coantic et al., 1981]. Assuming a logarithmic wind profile and neutral conditions, Monin and Obukhov [1954] scaling allows evaluation of friction velocity $u*$, roughness length z_0, and U_{10} , from the measured $U(z)$ profiles values with:

$$U(z) = \frac{u*}{\kappa} \ln \frac{z}{z_0} \tag{29}$$

where $\kappa = 0.41$ is the von Kármán constant, z is the measurement height above mean water level. The logarithmic profile is the solution of the horizontal momentum equations for the near-surface boundary

Run	h m	f_0 Hz	L_0 m	k_0h	$(ak)_0$	U_{10} m/s
1	0.14	1.7	0.51	1.78	0.120	3.18
2	0.14	1.7	0.51	1.78	0.121	5.58
3	0.14	1.2	0.85	1.07	0.100	5.70
4	0.26	1.7	0.54	3.03	0.124	3.39
5	0.26	1.7	0.54	3.03	0.124	5.10
6	0.26	1.4	0.77	2.10	0.166	3.46
7	0.26	1.4	0.77	2.10	0.168	5.43
8	0.48	1.7	0.54	5.58	0.091	5.70
9	0.48	1.4	0.80	3.79	0.126	5.71
10	0.48	1.1	1.27	2.38	0.119	3.60
11	0.74	1.7	0.54	8.59	0.026	3.96
12	0.74	1.7	0.54	8.59	0.026	5.79
13	0.74	1.7	0.54	8.59	0.034	3.92
14	0.74	1.7	0.54	8.59	0.034	5.79
15	0.74	1.4	0.80	5.83	0.051	5.81

Table 1: Experimental conditions. h is the water depth, f_0 is the paddle wave frequency, L_0 is the wavelength of the paddle waves, $(ak)_0$ is the steepness of the paddle waves measured without wind at fetch x_0, U_{10} is the wind speed extrapolated to the standard altitude of 10m.

sublayer dominated by friction forces, both viscous and turbulent [Komen, 1994] $\partial\tau/\partial z = 0$, with τ the momentum flux from air to water. A linear fit between $\ln z$ and $U(z)$ gives easily an estimation of $u*$ and z_0. Once $u*$ and z_0 are evaluated, U_{10} is taken as :

$$U_{10} = \frac{u*}{\kappa} \ln \frac{10}{z_0} \tag{30}$$

This method, called the "profile method", is routinely used for wind parameter determination in this facility (see for example recent papers of [Villefer et al., 2021; Bruch et al., 2021] where vertical wind profiles are displayed with $u*$, z_0, and U_{10} determinations). Two examples of vertical wind profiles are plotted in Figure (5). We did several times the same runs to estimate the precision on $u*$ and z_0. The relative precision was estimated to be 15% for $u*$ and U_{10} and 30% for z_0: $\frac{du*}{u*} = 15\%$, $\frac{dU_{10}}{U_{10}} = 15\%$, $\frac{dz_0}{z_0} = 30\%$. The estimated values of $u*$, U_{10}, and z_0 for the 15 different runs are listed in Table 2.

The drag coefficient $C_{d10} = \frac{\rho_a {u*}^2}{\rho_a U_{10}^2} = (\frac{u*}{U_{10}})^2$, with ρ_a the air density, is a commonly used parameter to characterise the shear air-flow above the waves and the non-dimensional momentum transfer from the air to the water. $\tau = \rho_a {u*}^2$ is the wind stress on the water surface. Values of C_{d10} for the 15 different runs are listed in Table 2.

In open seas, it is very difficult to measure z_0. A simple parametrization like : $z_0 = \alpha_{Ch}\, {u*}^2 / g$, with g the acceleration due to gravity, and α_{Ch} the Charnock parameter could be used to estimate z_0 from $u*$ [Charnock, 1955]. Values of α_{Ch} for the 15 runs are listed in Table 2

3.3.2. Wave parameters

The goal of the experiments was to measure the spatial and temporal growth rates of mechanical monochromatic waves forced by wind for different water depth conditions and to compare these growth rates with the theoretical values of [Montalvo et al., 2013 a]. An example of time series of the water elevation recorded by wave gauges during run 5 at fetch $x_0 = 20.1$ m, without wind and with wind on ($U_{10} = 5.10$ m/s is shown on Figure (6). The amplification by the wind of the dominant waves appears clearly on the plot. Looking at Figure (6) it seems possible to compute directly a *temporal*

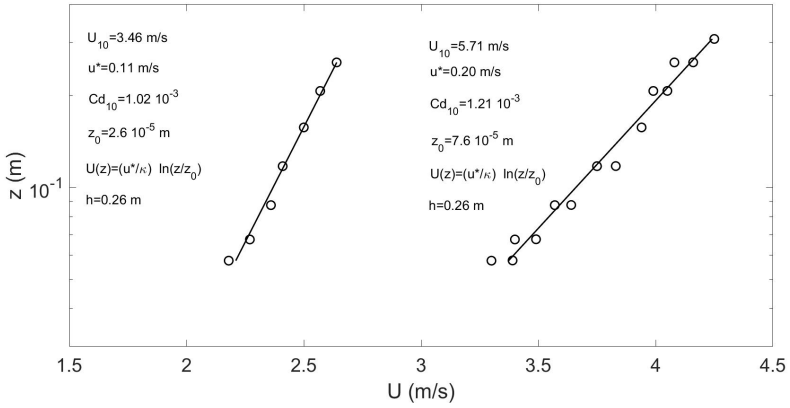

Figure 5: Two examples of logarithmic vertical wind profiles, with the estimated $u*$ and z_0 values (runs 6 and 9). z is the altitude above the mean water level.

Run	$u*$	z_0	C_{d10}	α_{Ch}
m/s	m/s	mm		
1	0.117	0.150	$1.36\ 10^{-3}$	$10.7\ 10^{-2}$
2	0.226	0.402	$1.64\ 10^{-3}$	$7.68\ 10^{-2}$
3	0.231	0.400	$1.64\ 10^{-3}$	$7.36\ 10^{-2}$
4	0.108	0.026	$1.02\ 10^{-3}$	$2.18\ 10^{-2}$
5	0.164	0.030	$1.04\ 10^{-3}$	$1.09\ 10^{-2}$
6	0.110	0.026	$1.02\ 10^{-3}$	$2.09\ 10^{-2}$
7	0.175	0.030	$1.04\ 10^{-3}$	$0.96\ 10^{-2}$
8	0.198	0.076	$1.21\ 10^{-3}$	$1.90\ 10^{-2}$
9	0.199	0.076	$1.21\ 10^{-3}$	$1.89\ 10^{-2}$
10	0.117	0.035	$1.07\ 10^{-3}$	$2.49\ 10^{-2}$
11	0.127	0.030	$1.04\ 10^{-3}$	$1.81\ 10^{-2}$
12	0.198	0.064	$1.18\ 10^{-3}$	$1.60\ 10^{-2}$
13	0.126	0.030	$1.04\ 10^{-3}$	$1.84\ 10^{-2}$
14	0.198	0.064	$1.18\ 10^{-3}$	$1.60\ 10^{-2}$
15	0.199	0.064	$1.18\ 10^{-3}$	$1.58\ 10^{-2}$

Table 2: Experimental conditions: $u*$ and z_0 are the friction velocity and roughness length estimated by the wind profile method, C_{d10} is the drag coefficient $C_{d10} = (u*/U_{10})^2$, α_{Ch} is the Charnock constant $\alpha_{Ch} = gz_0/u*^2$.

wave growth instead of a *spatial wave growth*. But it does not work for a few reasons: a) turning the wind "on" (from 0.0 m/s to, say, 5.1 m/s) takes time: it is not possible to command the wind turbine motor with a voltage step, it needs to be done progressively, and consequently the temporal growth will depend also on the wind gradient used to turn the wind on for the experiment at the beginning of the run; b) in a wave tank, in each location, the equilibrium state is reached quite rapidly, and in presence of low frequency mechanical waves, there are not enough waves before the equilibrium state to have a statistical good estimation of the temporal growth rate; c) It is difficult to determine the quantity $\frac{da}{dt}$ (with a the amplitude of the waves) in a wavy surface environment, more particularly if the wave spectrum is not narrow, i.e. with wind on.

Wave amplification factors with the respective effect of wind and depth will be discussed in section 4.2 .

An example of the energy density spectra of the waves recorded during run 5 is displayed in Figure (7). The spectra are plotted at fetches $x_0 = 2.4$ m and $x_1 = 20.1$ m, when there is no wind and when the wind is on. Wind waves appear clearly on spectra (d) at high frequencies, and only the second

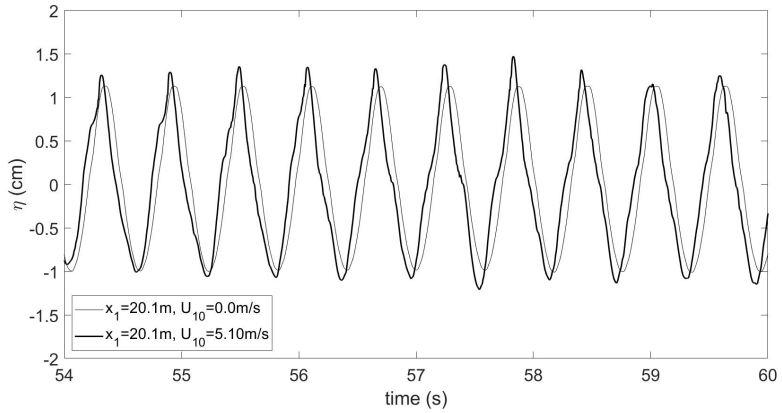

Figure 6: Example of time series of water elevation recorded by the wave gauges during run 5 at fetch $x_1 = 20.1$ m, without wind and with wind on.

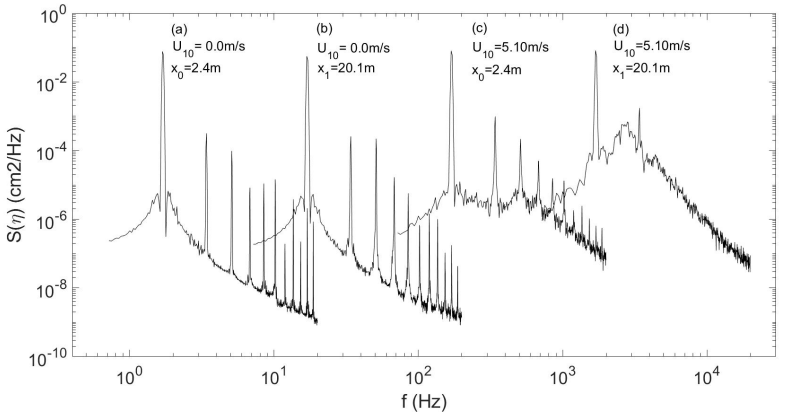

Figure 7: Density energy spectra of recorded waves during run 5. (a) fetch $x_0 = 2.4$ m no wind; (b) $x_1 = 20.1$ m no wind , with axis frequency multiplied by 10; (c) $x_0 = 2.4$ m $U_{10} = 5.10$ m/s , with axis frequency multiplied by 10^2; (d) $x_1 = 20.1$ m $U_{10} = 5.10$ m , with axis frequency multiplied by 10^3.

harmonics of the dominant waves are visible at fetch x_1 when wind is blowing.

In equations (23), (24) and (25), a_0 and a_1 are not the amplitude of each individual waves, but they must be considered as the average amplitude of waves with frequency close to the frequency f_0, the initial frequency of the wavemaker.

The determination of the amplitude a of the paddle waves, at the location of the wave gauges, was computed from the recorded time series of the wave gauges. We did a standard up-zero crossing analysis to separate each individual wave. Only the waves with a frequency f ranging between $0.8f_0 < f < 1.2f_0$ were considered to avoid noisy short wave or long wave perturbations and to focus on the mono-frequency generated waves. For each wave number i, the amplitude a_i was determined as half the crest-to-trough height of the wave number i :

$$a_i = \frac{(H_{max} - H_{min})_i}{2} \tag{31}$$

The mean amplitude $\bar{a}$ was computed as :

$$\bar{a} = \frac{1}{N} \sum_{i=1}^{N} a_i \tag{32}$$

with N the total number of waves of the run.

The experimental non-dimensional temporal wave growths were estimated using equations (23), (24) and (25), with $\bar{a_1}$ and $\bar{a_0}$ instead of a_1 and a_0, and with $x_1 = 20.1$ m, $x_0 = 2.4$ m.

3.4. Measured values and precision of the measurements

Main parameters of the 15 runs were listed in Table 1. Other environmental parameters defined in sections 3.3.1 and 3.3.2 which were computed from wind and wave measurements are listed in Table 2. Friction velocity $u*$ ranged from 0.108 m/s to 0.231 m/s, roughness length z_0 from 0.030 mm to 0.402 mm. The drag coefficient C_{d10} ranged from 1.0210^{-3} to 1.6410^{-3}, and the Charnock constant α_{Ch} from 0.0096 to 0.107.

In the following paragraphs, we will consider non-dimensional variables which may be active in fetch or duration limited growth. Like in [Sverdrup and Munk, 1947; Kitaigorodskii, 1970; Young, 1999] these quantities are the non-dimensional energy $\frac{g^2\sigma^2}{U_{10}^4}$, with σ the standard deviation of the water elevation, the non-dimensional frequency $\frac{f_0 U_{10}}{g}$, the non-dimensional depth $\frac{gh}{U_{10}}$, the inverse wave age $\frac{U_{10}}{c}$.

It is quite important to evaluate the precision of the measurements and the errors made on the environmental parameters computed from the raw data acquired during the experiments. A good comparison with theory may be done only if the uncertainties on measured data are clearly given. By doing the same experiment several times, we have estimated the relative errors on the measurements we conducted in the facility. All the estimations and error computations are detailed in Appendix A. Relative errors on the different parameters are summarized in Table 3.

x	h	f_0	c_0	C_{g0}	L_0	$k_0 h$	$\bar{a}$	σ	$(ak)_0$	$u*$	z_0
0.5%	1%	2%	2%	6%	4%	5%	8%	8%	12%	15%	30%

U_{10}	C_{d10}	α_{Ch}	δ	θ_{dw}	θ_{fd}	$\hat{\gamma}_{et}$	β	γ_{et}/f_0
15%	60%	60%	31%	17%	19.5%	54%	75%	41%

U_{10}/c_0	gh/U_{10}^2	$f_0 U_{10}/g$	$g^2\,\sigma^2/U_{10}^4$
17%	31%	17%	76%

Table 3: Relative errors on estimated values.

The measured values of $(\bar{a_0})_{|U_0}$, $(\bar{a_0})_{|U_{ref}}$, $(\bar{a_1})_{|U_0}$, $(\bar{a_1})_{|U_{ref}}$ are displayed in Table 4, as well as the estimated wave celerity c_0 (relation (27)), wave group velocity C_{g0} (relation (28)), wave age $c_0/u*$, and non-dimensional parameters δ, θ_{dw}, θ_{fd} (relation (8)), $\hat{\gamma}_{et}$ (relation (23)), β (relation (24)) and γ_{et}/f_0 (relation (25)). Parameter δ ranges between 4.7 to 76.0 and parameter θ_{fd} ranges between 1.6 to 4.9. Amplification factor β ranges between 0.10 (quite no amplification) to 17.0 (large amplification)

4. Discussion

4.1. Depth influence on air-to-water transfers

4.1.1. Depth influence on drag coefficient C_d

Figure (8) shows the evolution of measured C_{d10} with estimated U_{10}. Drag coefficients in low water depth environment ($kh < 1.8$) are clearly higher than those in large depth configurations. In open

Run	$(\bar{a_0})_{\|U_0}$	$(\bar{a_0})_{\|U_{ref}}$	$(\bar{a_1})_{\|U_0}$	$(\bar{a_1})_{\|U_{ref}}$	c_0	C_{g0}	$c_0/u*$	δ	θ_{dw}	θ_{fd}	$\hat{\gamma}_{et}$	β	γ_{et}/f_0
	cm	cm	cm	cm	m/s	m/s					$*10^{-5}$		$*10^{-4}$
1	0.97	0.95	0.78	0.80	0.87	0.52	7.4	17	3.1	3.0	0.71	0.34	1.4
2	0.99	1.03	0.79	1.00	0.87	0.52	3.8	4.7	1.6	1.6	36	2.5	38
3	1.36	1.55	0.80	0.81	1.03	0.78	4.4	4.5	2.0	1.8	0.20	0.10	0.3
4	1.06	1.07	0.87	0.96	0.91	0.47	8.5	36	3.5	3.5	8.1	5.5	18
5	1.06	1.13	0.87	1.19	0.91	0.47	5.6	16	2.3	2.3	30	5.9	44
6	2.04	2.29	1.60	1.83	1.08	0.61	9.8	35	4.1	4.0	2.1	2.3	5.4
7	2.07	2.12	1.63	1.84	1.08	0.61	6.2	14	2.6	2.5	18	4.9	30
8	0.79	0.63	0.51	0.89	0.91	0.46	4.6	20	1.9	1.9	10	12	128
9	1.59	1.74	1.35	1.49	1.11	0.56	5.6	20	2.3	2.3	2.0	0.39	2.9
10	2.41	2.42	2.30	2.39	1.40	0.75	11.9	57	4.9	4.9	4.2	7.9	13
11	0.22	0.25	0.25	0.65	0.92	0.46	7.2	75	3.0	3.0	40	17	75
12	0.22	0.24	0.25	0.92	0.92	0.46	4.6	31	1.9	1.9	79	8.8	94
13	0.30	0.37	0.39	0.83	0.92	0.46	7.3	76	3.0	3.0	25	11	47
14	0.30	0.30	0.39	0.88	0.92	0.46	4.6	31	1.9	1.9	52	5.8	62
15	0.65	1.04	0.48	1.08	1.12	0.56	5.6	31	2.3	2.3	63	12	91

Table 4: Experimental measured values: mean wave amplitudes at fetch x_0 without wind $(\bar{a_0})_{|U_0}$ and with wind $(\bar{a_0})_{|U_{ref}}$, and at fetch x_1 without wind $(\bar{a_1})_{|U_0}$ and with wind $(\bar{a_1})_{|U_{ref}}$. Estimated values: celerity c_0, group velocity C_{g0}, wave age $c_0/u*$, non-dimensional parameters δ, θ_{dw}, θ_{fd}, $\hat{\gamma}_{et}$, β and γ_{et}/f_0.

seas, when U_{10} is known from satellite or models, a model of the drag like : $C_{d10} = a + b\,U_{10}$, a and b being constant, is widely used to estimate $u*$ from U_{10} : $u* = U_{10}\,(C_{d10})^{0.5}$. A quite large range of a and b values have been reported from measurements like, for example : $a = 0.75\,10^{-3}, b = 0.067\,10^{-3}$ [Garratt, 1977]; $a = 0.61\,10^{-3}, b = 0.063\,10^{-3}$ [Smith, 1980]; $a = 0.80\,10^{-3}, b = 0.065\,10^{-3}$ [Wu, 1982]; $a = 0.96\,10^{-3}, b = 0.041\,10^{-3}$ [Donelan, 1982]; $a = 0.58\,10^{-3}, b = 0.084\,10^{-3}$ [Geernaert, 1987]; $a = 0.49\,10^{-3}, b = 0.071\,10^{-3}$ [Anderson, 1993]; $a = 0.50\,10^{-3}, b = 0.071\,10^{-3}$ [Yelland et al., 1998]; $a = 0.96\,10^{-3}, b = 0.060\,10^{-3}$ [Toffoli et al., 2012]. Our measured trend of C_{d10} with U_{10} is equivalent to the trend observed in literature (i.e. the same as [Smith, 1980]: $b = 0.063\,10^{-3}$) for large depth configuration. But for low depth, C_{d10} values are significantly higher and the trend is much higher : $b = 0.112\,10^{-3}$.

[Bi et al., 2015] investigated the drag coefficient C_d in the South China Sea from 2008 to 2014, and one of their towers to collect data was located in 15 m of water. Some of their data were considered to be in finite depth environment (i.e. depth lower than half the dominant wavelength, i.e. $kh < \pi$). [Bi et al., 2015] found that the drag coefficient was higher in shallow water by 40% for $U_{10} < 10$ m/s. Jimenez and Dudhia [2018] showed that the drag at the location of FINO1 offshore platform in shallow waters was about 30% higher than the drag in deep waters. Very close to the shore, the drag coefficients over the surf zone during onshore winds were determined by Shabani et al. [2014] to be almost 200% the values expected at the same wind speed and open ocean conditions ! [Anctil and Donelan, 1986] found that the wind dependence of C_d derived for shallow water differs from that of deep water. sometimes, their C_d values were 40% to 80% higher for shallow water. They explain the modification of C_d by the modification of wave age c/U_{10} and modification of the root mean square wave slope by the bottom effect on waves in shallow water. The geometric shape of the wave and the kinematics are modified by shoaling effects, thus modifying air-water transfers. [Toffoli et al., 2012] argued that water depth effects together with large wind result in a steeper and more vertically asymmetric profile for dominant waves, which enhances breaking probability, air flow separation and sea drag. They proposed a parametrisation of C_d with an inverse quadratic function of a non-linear parameter μ depending on both wave steepness and water depth. In our figure(8) we see that our Drag coefficient is 45% higher at low water depth ($kh < 1.8$) if compared to higher water depth ($kh > 2.0$). We notice also that the higher wind speed, the higher relative difference between C_d values at low depth and C_d values at large depth.

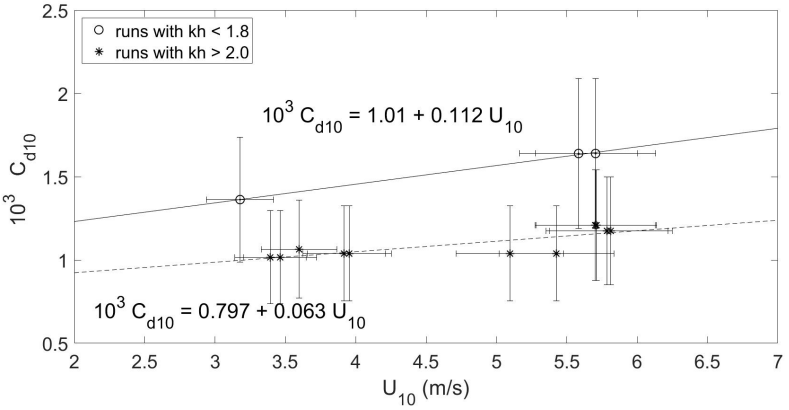

Figure 8: Drag coefficient C_{d10} as function of U_{10}. Drag coefficients are higher for low water depth (i.e $kh < 1.8$)

[Zhao et al., 2015] explored also C_d in the South China Sea from wind propeller anemometers stationed on a coastal observation tower (water depth 14 m), to observe the effect of water depth on C_d. But their study was more focused on typhoon measurements. [Zhao et al., 2015] concluded that water depth unequivocally affects the drag coefficient when compared to deep open ocean results, but more particularly at high winds ($U_{10} > 15$ m/s), which is beyond our scope here. They found that in shallow water depth environment, the C_d maximum occurs approximately at 24 m/s, which is 5 to 15 m/s lower than that of the open sea.This is prospectively due to wave shoaling and wave breaking conditions pertaining to the shallow water in high wind conditions. [Zhao et al., 2015] proposed a C_d formulation as a function of wind speed and water depth, but in their formulation, the water depth plays a role only in the $U_{10} > 15$ m/s part of the C_d curves. Before them, [Geernaert et al., 1986] have also shown that the shallow water C_d values for wind speeds above 15 m/s are higher than those over the open ocean and they attributed the difference to the variations in the surface wave energy spectrum. Based on their air-flow separation model, [Makin and Kudryavtsev, 2002] and their WOWC (Wind Over Waves Coupling) model have reproduced the increase in C_d with decreasing water depth: at moderate and high winds, decreasing water depth induces a steepening of dominant waves and thus more air-flow separation at the crest of the waves, and more drag. Makin et al. [2004] explained the wind speed, wave age and finite depth dependences of the sea drag in a wave tank environment with this model.

What is new in our measurements, is the fact that we find a significant increase of C_d, even at relatively low wind speed (i.e. $U_{10} < 6$ m/s). [Donelan, 1982; Oost et al., 2002; Gao et al., 2009; Toffoli et al., 2012] have also shown that the C_d over shallow water is higher than that over deep water at the same wind speed, but they have related this phenomenon to wave state parameters, e.g., wave age and wave steepness. They do not include water depth h or non-dimensional parameter kh in their drag model.

4.1.2. Depth influence on aerodynamic roughness length z_0

The evolution of z_0 with the wind U_{10} is shown on figure (9). z_0 values are much higher for low water depths (i.e $kh < 1.8$) than for greater depths ($kh < 2.0$), and the variation trend of z_0 with U_{10} is six times higher for low depth than deep water. Recently [Jimenez and Dudhia, 2018] pointed out the need to modify the sea surface roughness formulation over shallow waters taking into account the water depth. [Anctil and Donelan, 1986] explained the increase of z_0 by the increase of the "inverse wave age" U_{10}/c, the increase of root mean square wave slope η_X, and the increase of significant wave height H_s due to shoaling effect near the coast in intermediate and shallow water conditions. They proposed a relationship like : $z_0 = a_1\, H_s\, (U_{10}/c)^{b_1}\, (\eta_X)^{c_1}$. [Smith et al., 1992] have suggested that

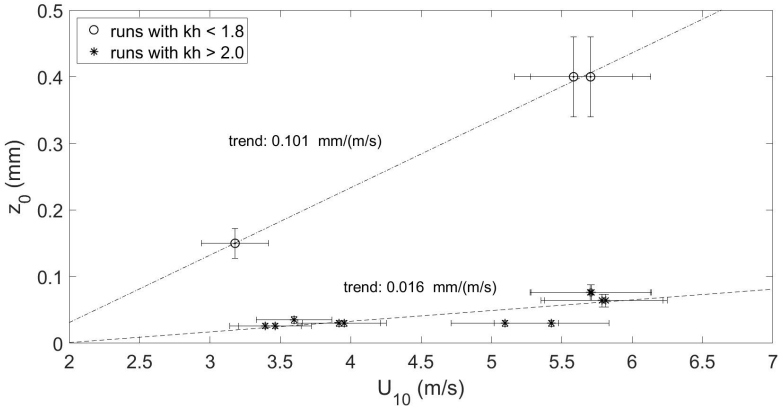

Figure 9: Roughness parameter z_0 as function of U_{10}. z_0 values are higher for low water depth (i.e $kh < 1.8$), and the trend is six times higher.

celerity and steepness are the wave properties more likely to influence the surface roughness z_0 in finite depth environment because celerity is restricted by water depth and wave age is shorter at short fetch. [Gao et al., 2009] using three different databases, illustrated the increase of z_0 with low depth, because the finite depth change the wave celerity c, and by the way the inverse wave age (U_{10}/c). They also proposed a model of z_0 with the inverse wave age U_{10}/c. [Oost et al., 2002] also took into account the wave steepness in their model of z_0, the waves being steeper when the depth is low, but they do not include parameter kh in the z_0 estimation. MacMahan [2017] related the increase of roughness length z_0 near the coasts in finite depth to surfzone foam coverage due to wave breaking. But in our experiment we did not observe wave breaking although roughness parameter z_0 was higher in low depth conditions.

4.1.3. Depth influence on Charnock parameter α_{Ch}

In open seas, the Charnock parameter α_{Ch} is generally assumed constant, although a range of values have been reported from measurements: 0.014 [Garratt, 1977], 0.018 [Wu, 1980], 0.019 [Geernaert et al., 1986], 0.035 [Kitaigorodskii and Volkov, 1965] among others. [Vickers and Mahrt, 1997] conducted measurements by fetch length and they measured $\alpha_{Ch} = 0.018$ for onshore and $\alpha_{Ch} = 0.073$ for offshore wind conditions during the RASEX campaign [Lüko et al., 2020], i.e. at very short fetches and intermediate water depths. Above the water surface in the intertidal area and in the inner-surf and swash zones, which means in very shallow water environment and even sometimes with no water but along the shoreline, during the Stradbroke 2012 campaign, [Shabani et al., 2014] observed Charnock coefficients an order of magnitude greater than open ocean values : the average Charnock coefficient of their data was $\alpha_{Ch} = 0.110$! To our knowledge, these are the highest observed α_{Ch} values so far. They explained this large increase of Charnock coefficients by the slower celerity in the surf zones, the breaking of the waves when they reach the shore and more particularly the sawtooth wave shape in the inner surf zone and swash zone, with asymmetric and very steep waves. From Lake George measurements, Toffoli et al. [2012] have proposed a parametrisation of α_{Ch} using an inverse quadratic function of a complex non-linear parameter μ depending on wave steepness and water depth.

Figure (10) shows the evolution of our estimated α_{Ch} data with the non-dimensional depth parameter kh. For high depth, our mean α_{Ch} value is 0.018, which is the same value reported by [Wu, 1980] and [Vickers and Mahrt, 1997]. This value of 0.018 was also proposed by [Charnock, 1955]. But for low depth configuration (i.e. $kh < 1.8$), α_{Ch} is 5 times higher: 0.086 . This value is slightly greater than the RASEX campaign Charnock value for offshore winds [Lüko et al., 2020], but slightly lower than the Stradbroke campaign value recorded along the shore line [Shabani et al., 2014]. However, one of our measurements (run 1, $\alpha_{Ch} = 0.107$) is close to equal to their mean recorded value: $\alpha_{Ch} = 0.110$. The depth effect on Charnock parameter appears clearly on our figure (10).

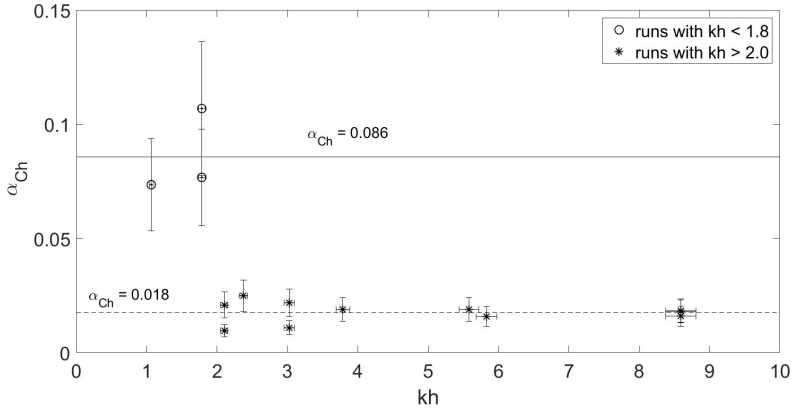

Figure 10: Charnock parameter $\alpha_{Ch} = \frac{g z_0}{u*^2}$ as function of non-dimensional depth parameter kh. α_{Ch} values are higher for low water depth (i.e $kh < 1.8$)

4.2. Depth influence on wave growth

[Montalvo et al., 2013 a,b] and [Latifi et al., 2017] have shown that the limit for which the growth rate $\hat{\gamma}_{et}$ goes to zero was defined by the equation $\theta_{fd}^c = \sqrt{\delta}$. Figure (11) shows the location of the 15 experiments in the (θ_{fd}, δ) plane, together with the [Montalvo et al., 2013 a] limit and the data of [Donelan et al., 2005, 2006], from the Australian Shallow Water Experiment. This figure shows the wide range of δ and θ_{fd} values covered by our experiments. Even if the relative errors are quite high, values remains below the physical limit for which sea state evolution (wave amplification) is not possible.

Figure (12) displays the evolution of the non-dimensional frequency $f_0 U_{10}/g$ with non-dimensional depth gh/U_{10}^2. This graph shows that are data are inside the asymptotic non-dimensional limit-law proposed by [Young and Verhagen, 1996 a; Young, 1997]: $\frac{f_0 U_{10}}{g} = 1.25(\frac{gh}{U_{10}^2})^{-0.45}$. Our data are closer to the [Young and Verhagen, 1996 a] limit than the [Bretschneider, 1958] limit: $\frac{f_0 U_{10}}{g} = 0.16(\frac{gh}{U_{10}^2})^{-0.375}$.

Figure (13) displays the evolution of the inverse wave age U_{10}/c_0 with non-dimensional depth gh/U_{10}^2. This graph shows that the low depth limits the wave age: the wave age cannot be beyond the non-dimensional depth asymptotic limit proposed by [Young, 1997]: $\frac{U_{10}}{c_0} = 1.25(\frac{gh}{U_{10}^2})^{-0.45}$.

Figure (14) displays the evolution of the non-dimensional energy $g^2\,\sigma^2/U_{10}^4$ with non-dimensional depth gh/U_{10}^2. This graph shows that our data are inside the asymptotic limit-laws proposed by [Young and Verhagen, 1996 a] : $\frac{g^2\sigma^2}{U_{10}^4} = 1.06\ 10^{-3}(\frac{gh}{U_{10}^2})^{1.3}$ and [Bretschneider, 1958; CERC, 1977] : $\frac{g^2\sigma^2}{U_{10}^4} = 1.40\ 10^{-3}(\frac{gh}{U_{10}^2})^{1.5}$. The low depth limits the total energy of the sea state. Waves cannot be amplified beyond a threshold value depending on the non-dimensional depth.

The non-dimensional growth rate $\hat{\gamma}_{et}$ is now compared in figure (15) with the theoretical curves of [Montalvo et al., 2013 a]. The existence of a finite depth h transforms the unique Miles curve of wave growth rate in deep water in a *family of curves* indexed by $\delta = gh/U_1^2$, i.e., a curve for each value of δ. Figure (15) shows a theoretical family of $\hat{\gamma}_{et}$ for four values of δ: $\delta_{th} = 4, 9, 25, 49$ against θ_{fd} parameter. In the same figure are plotted the experimental values of $\hat{\gamma}_{et}$. These data are partitioned into four ranges of δ i.e., $\delta \in [0 \quad 6.5], [6.5 \quad 21], [21 \quad 36], [36 \quad \infty]$. Small finite values of θ_{fd} correspond to short surface waves characterizing young wind waves. For time increasing the wave age θ_{fd} increases which

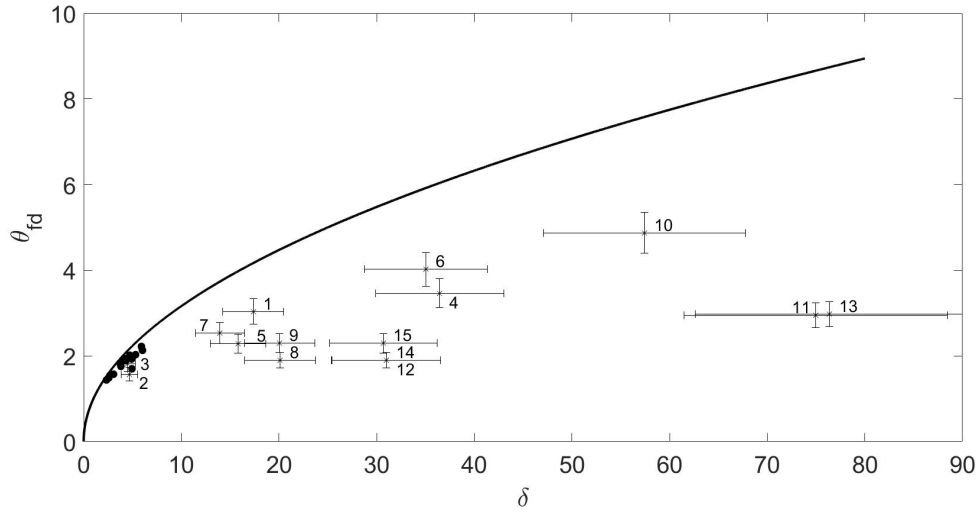

Figure 11: Location in the (θ_{fd}, δ) plane of the 15 runs. Each run number is printed at its location with the corresponding error bars. The black line is the [Montalvo et al., 2013 a] limit (location of the critical θ^c_{fd} values) where there is no amplification by the wind. Black dots are the points from the Australian Shallow Water Experiment [Donelan et al., 2006].

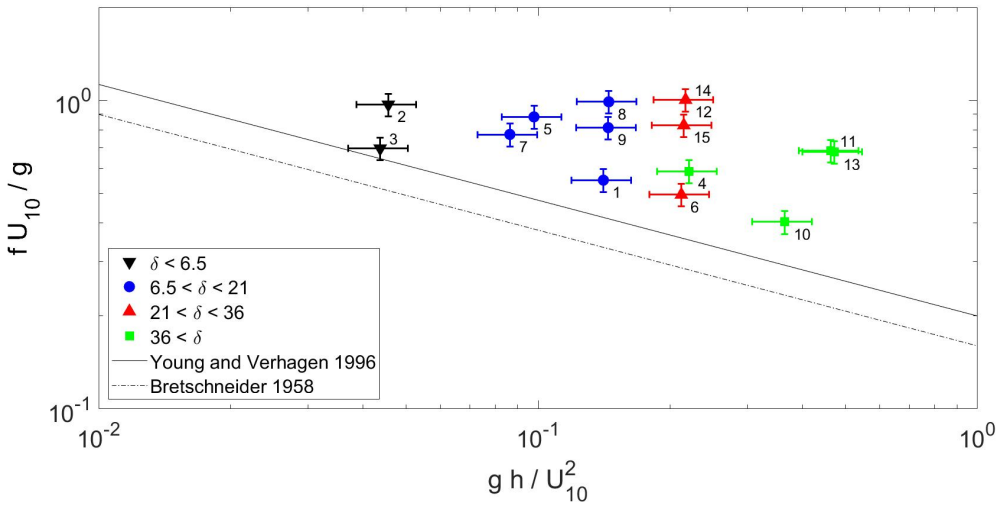

Figure 12: Non-dimensional frequency $f_0 U_{10}/g$ evolution with the non-dimensional depth gh/U^2_{10}. Run numbers are written on the plot. Full symbols with error bars : measured values for $\delta \in [0\ 6.5]$ (▼), $\delta \in [6.5\ 21]$ (●), $\delta \in [21\ 36]$ (▲), $\delta \in [36\ \infty]$(■). Straight black line: [Young and Verhagen, 1996 a] depth asymptotic limit : $\frac{f_0 U_{10}}{g} = 0.20(\frac{gh}{U^2_{10}})^{-0.375}$; Straight dotted line: [Bretschneider, 1958] limit : $\frac{f_0 U_{10}}{g} = 0.16(\frac{gh}{U^2_{10}})^{-0.375}$.

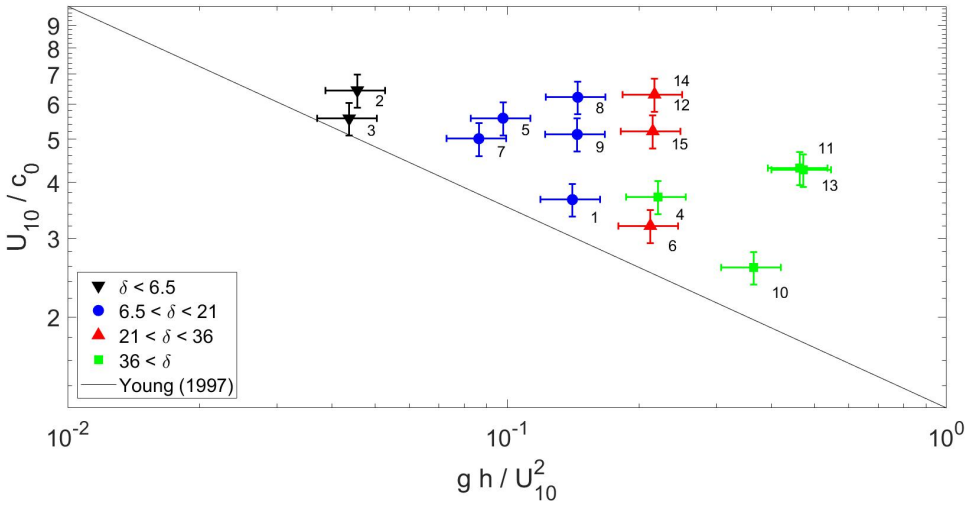

Figure 13: Inverse wave age U_{10}/c_0 evolution with the non-dimensional depth $gh/(U_{10}^2)$. Run numbers are written on the plot. Full symbols with error bars : measured values for $\delta \in [0\ 6.5]$ (▼), $\delta \in [6.5\ 21]$ (●), $\delta \in [21\ 36]$ (▲), $\delta \in [36\ \infty]$(■). Straight black line: [Young, 1997] limit : $\frac{U_{10}}{c_0} = 1.25(\frac{gd}{U_{10}^2})^{-0.45}$.

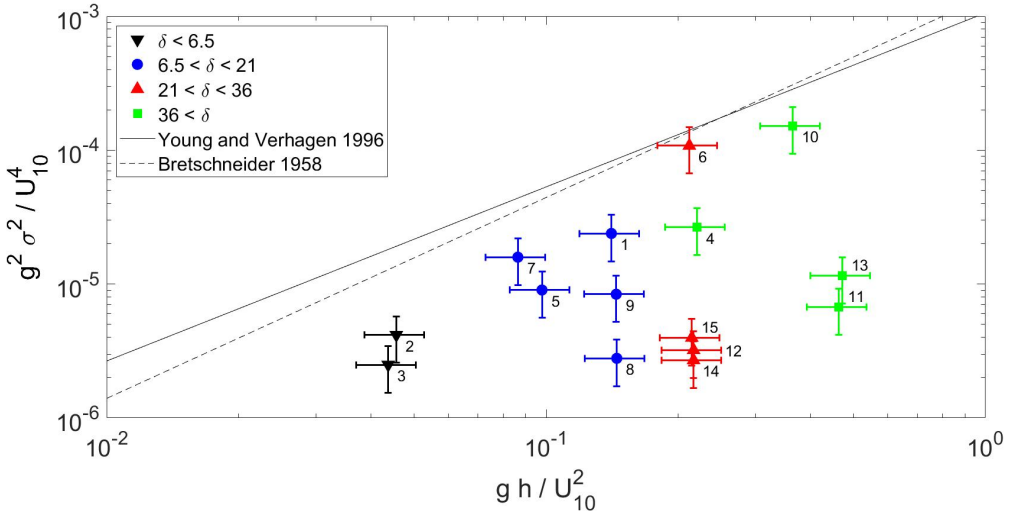

Figure 14: Non-dimensional energy $g^2\,\sigma^2/U_{10}^4$ evolution with the non-dimensional depth $gh/(U_{10}^2)$. Run numbers are written on the plot. Full symbols with error bars : measured values for $\delta \in [0\ \ 6.5]$ (▼), $\delta \in [6.5\ \ 21]$ (●), $\delta \in [21\ \ 36]$ (▲), $\delta \in [36\ \ \infty]$(■). Straight black line: [Young and Verhagen, 1996 a] limit : $\frac{g^2\,\sigma^2}{U_{10}^4} = 1.06\ 10^{-3}(\frac{gh}{U_{10}^2})^{1.3}$; Straight dotted line: [Bretschneider, 1958; CERC, 1977] limit : $\frac{g^2\,\sigma^2}{U_{10}^4} = 1.40\ 10^{-3}(\frac{gh}{U_{10}^2})^{1.5}$.

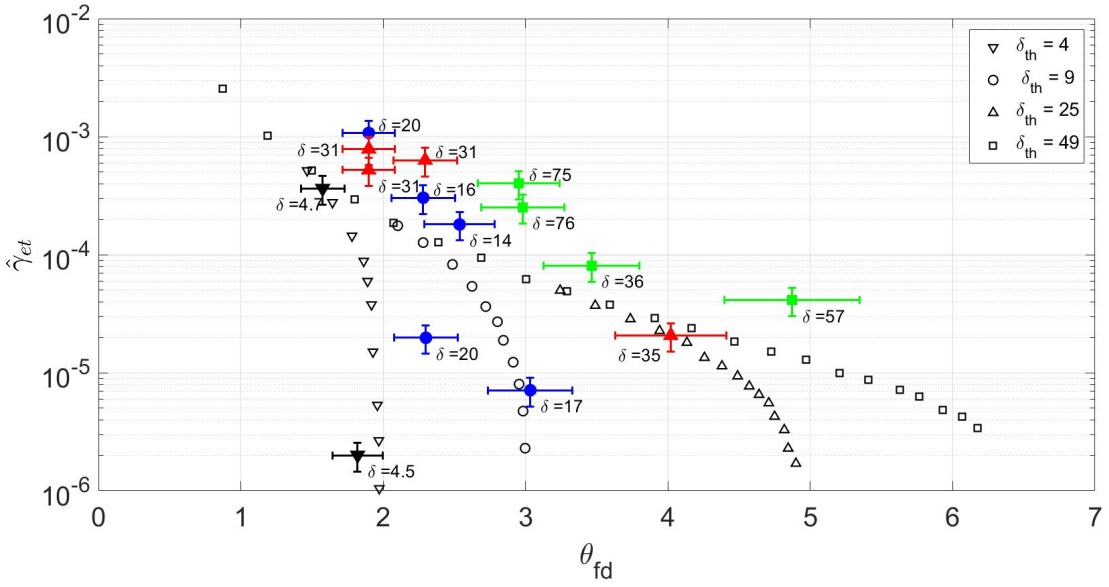

Figure 15: Comparison of the non-dimensional growth rate $\hat{\gamma}_{et}$ values measured in the facility with the theoretical curves of [Montalvo et al., 2013 a]. Empty symbols: theoretical values for $\delta_{th} = 4$ (∇), $\delta_{th} = 9$ ($\circ$), $\delta_{th} = 25$ ($\triangle$), $\delta_{th} = 49$ ($\square$). Full symbols with error bars : measured values for $\delta \in [0\ 6.5]$ ($\blacktriangledown$), $\delta \in [6.5\ 21]$ ($\bullet$), $\delta \in [21\ 36]$ ($\blacktriangle$), $\delta \in [36\ \infty]$($\blacksquare$). The value of δ for each experimental run is written inside the figure.

corresponds to mild or moderate wavelengths. The waves develop and the growth rate $\hat{\gamma}_{et}$ gradually decreases due to the effects of finite depth. As $\hat{\gamma}_{et}$ goes to zero, each δ-curve approaches the theoretical θ_{fd}*-limited growth,* θ^c_{fd}, given by $\theta^c_{fd} = \delta^{0.5}$. Hence for $\delta_{th} = 4, 9, 25, 49$ the values of θ^c_{fd} for $\hat{\gamma}_{et}$ are: $\theta^c_{fd} = 2, 3, 5, 7$. The wave reaches a final state of linear progressive wave with zero growth. In other words, for a given δ the surface wave does not grow old any more beyond a determined θ^c_{fd}.

The experimental measurements follow more or less the general tendencies of the theoretical curves: a) the grow rate is lower for low values of δ and large values of θ_{fd}; b) the growth rate with low δ can be sometimes two orders of magnitude lower than run with higher δ. c) usually, but not always, experimental values of $\hat{\gamma}_{et}$ are higher than the theoretical values. If we draw linear regression lines for several bins of δ values, we find however a good general trend of the experimental measurements with a decrease towards no amplification at high θ_{fd} and low δ. These regression lines are drawn in figure (16). The intersection of the regression lines with quite zero non-dimensional growth-rate (here $\hat{\gamma}_{et} = 10^{-6}$) gives the critical θ^c_{fd} experimental value for the bin of δ data considered, and thus the corresponding $\delta^c = (\theta^c_{fd})^2$ value. We note that for each bin of δ, the critical δ^c belongs to that bin : $3.42 \in [0\ 6.5]$, $12.7 \in [6.5\ 21]$, $34.3 \in [21\ 36]$, $68.6 \in [36\ \infty]$. This decrease towards zero amplification at θ^c_{fd} was the key point developed by the [Montalvo et al., 2013 a,b; Latifi et al., 2017] theory. It is the first time that such a theory is illustrated by wave tank experiments.

In order to compare the measured wave growth with previous well known experiments, we have plotted our computed values of γ_{et}/f_0 versus inverse wave age $u*/c_0$ in figure (17), together with data compiled by [Plant, 1982], as they are shown in figure 4.2, page 52 of [Young, 1997]. Data came from [Larson and Wright, 1975; Wu et al., 1977, 1979; Snyder et al., 1981; Shemdin and Hsu, 1967]. We see clearly that some of measured growth rates are right in the [Plant, 1982] tendency, lying along Miles and [Snyder et al., 1981] curves, but others are completely below the proposed range, close to zero amplification. As we saw before, according to [Montalvo et al., 2013 a] theory, this happens because δ is not high and θ_{fd} is not small. In shallow water environment, amplification factor by the wind may

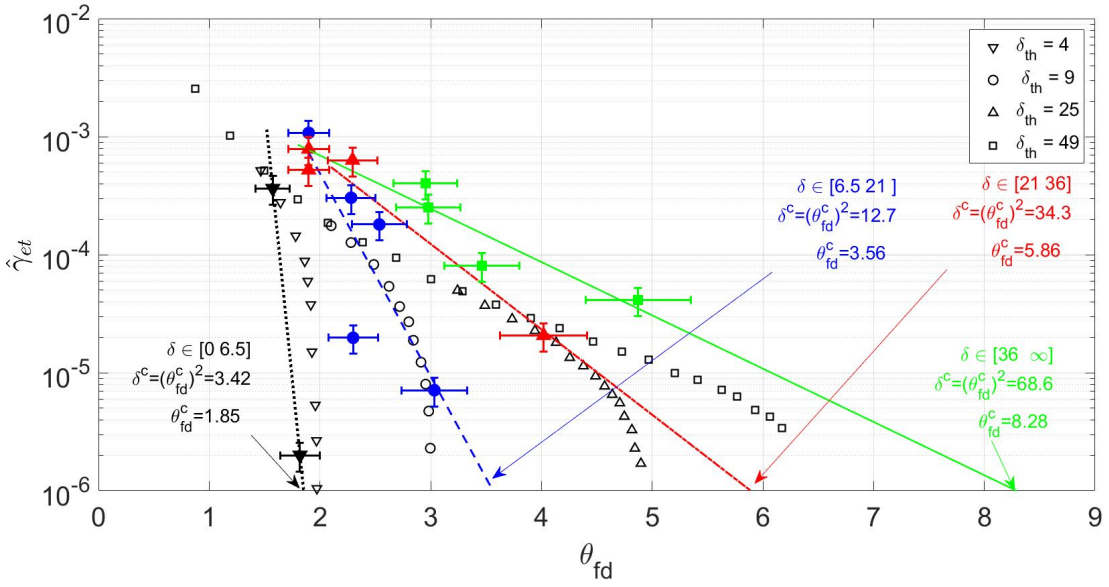

Figure 16: Same as figure (15), but we have added linear regression lines between $\log_{10}\hat{\gamma}_{et}$ and θ_{fd}. Empty symbols: theoretical values for $\delta_{th} = 4(\nabla)$, $\delta_{th} = 9(\circ)$, $\delta_{th} = 25(\triangle)$, $\delta_{th} = 49(\square)$. Full symbols and regression lines: experimental values: dotted line and ($\blacktriangledown$) : $\delta \in [0\ \ 6.5]$, dashed line and ($\bullet$), $\delta \in [21\ \ 36]$ ($\blacktriangle$), $\delta \in [36\ \ \infty]$($\blacksquare$) : $\delta \in [36\ \ \infty]$. The critical experimental values of θ^c_{fd} and δ^c for which there is no amplification ($\hat{\gamma}_{et} = 10^{-6}$) by bins of δ are written in the figure.

be sometimes not efficient.

The comparison between the non-dimensional experimental β Miles parameter and the theoretical ones of [Montalvo et al., 2013 a] is shown in figure (18). Some measured β values seem much higher than theoretical β values. We have done those runs several times and we always found these large β values. In fact, those values seem high in comparison with the [Montalvo et al., 2013 a] theory, but they are not so high if we compare them to previous experimental studies done in the past on the wave growth of wind waves, as shown on figure(19). Our β values are more or less on the lower part of the figure, and we see clearly that some values are very close to zero, if compared with previous published data. In another paper [Troitskaya et al., 2018], figure (2-c), all the β values computed from a precise DNS model, and also by a quasi-linear model of waves amplified by wind, are all above 20, i.e. above our β measured data.

Regression lines between β and θ_{fd}, for several bins of δ values, are shown in figure(20). The intersection of these lines with the $\beta = 0$ axis gives the critical θ^c_{fd} experimental value for the bin of δ data considered, and thus the corresponding $\delta^c = (\theta^c_{fd})^2$ value. Like in figure(16), we note again that for each bin of δ, the critical δ^c belongs to that bin : $3.3 \in [0\ \ 6.5]$, $8.6 \in [6.5\ \ 21]$, $26.0 \in [21\ \ 36]$, $50.4 \in [36\ \ \infty]$. This experiment shows that, following [Montalvo et al., 2013 a,b; Latifi et al., 2017] development, wind-wave growth rate by Miles's mechanism in finite water depth environment could be very low.

5. Conclusions

Experiments were conducted in a wind-wave facility to study momentum transfer from air to water and the growth rate of the waves by the wind for different configurations of water depth. Fifteen different runs were done. Some runs were done many times to check the uncertainties on the measurements. All the error bars on the different graphs were plotted. Wind speeds and wave steepnesses

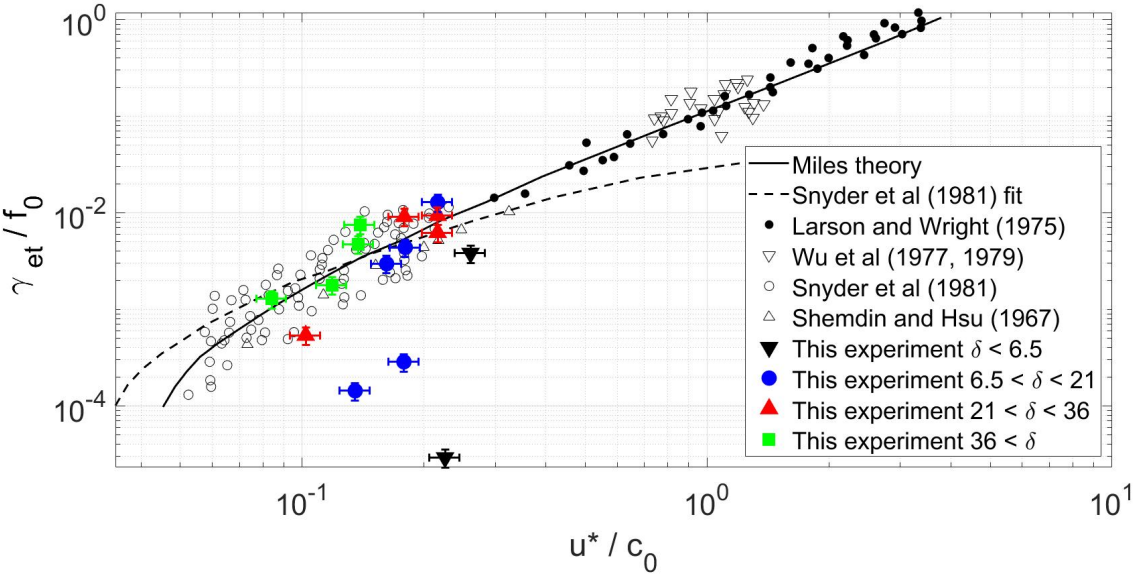

Figure 17: Non-dimensional growth rate γ_{et}/f_0 versus inverse wave age $u*/c_0$. Solid symbols : our experiment. Open symbols : other experiments, data gathered by [Plant, 1982] and displayed in [Young, 1997] page 52 (see also [Snyder et al., 1981; Larson and Wright, 1975; Wu et al., 1977, 1979; Shemdin and Hsu, 1967]). Solid line: Miles Theory, Dashed line : [Snyder et al., 1981] interpolation.

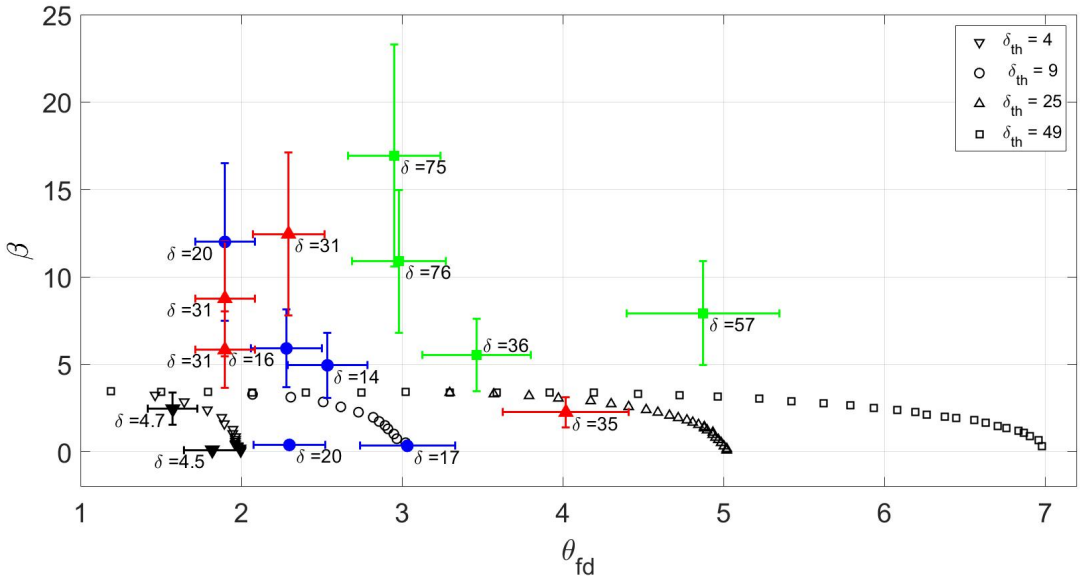

Figure 18: Comparison of the non-dimensional growth rate β measured in the facility with the theoretical curves of [Montalvo et al., 2013 a]. Empty symbols: β theoretical values for $\delta_{th} = 4$ (∇), $\delta_{th} = 9$ ($\circ$), $\delta_{th} = 25$ ($\triangle$), $\delta_{th} = 49$ ($\square$). Full symbols with error bars : β measured values for $\delta \in [0\ \ 6.5]$ ($\blacktriangledown$), $\delta \in [6.5\ \ 21]$ ($\bullet$), $\delta \in [21\ \ 36]$ ($\blacktriangle$), $\delta \in [36\ \ \infty]$($\blacksquare$). The value of δ for each experimental run is written in the figure.

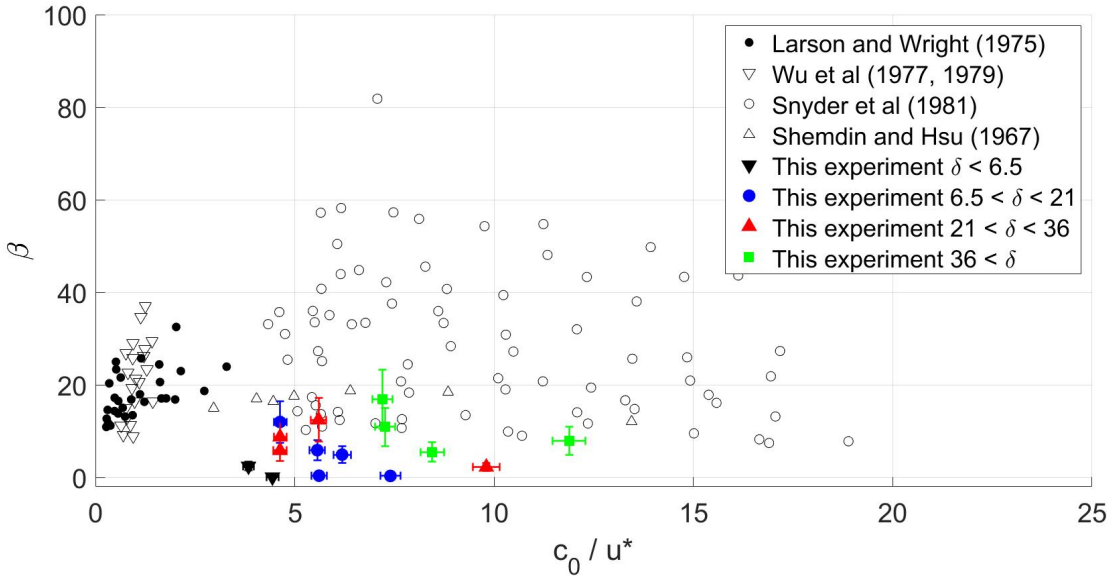

Figure 19: Non-dimensional growth rate β versus wave age $c_0/u*$. Solid symbols : our experiment. Open symbols : other experiments (see legend), data gathered by [Plant, 1982] and displayed in [Young, 1997] page 53 (see also [Snyder et al., 1981; Larson and Wright, 1975; Wu et al., 1977, 1979; Shemdin and Hsu, 1967]).

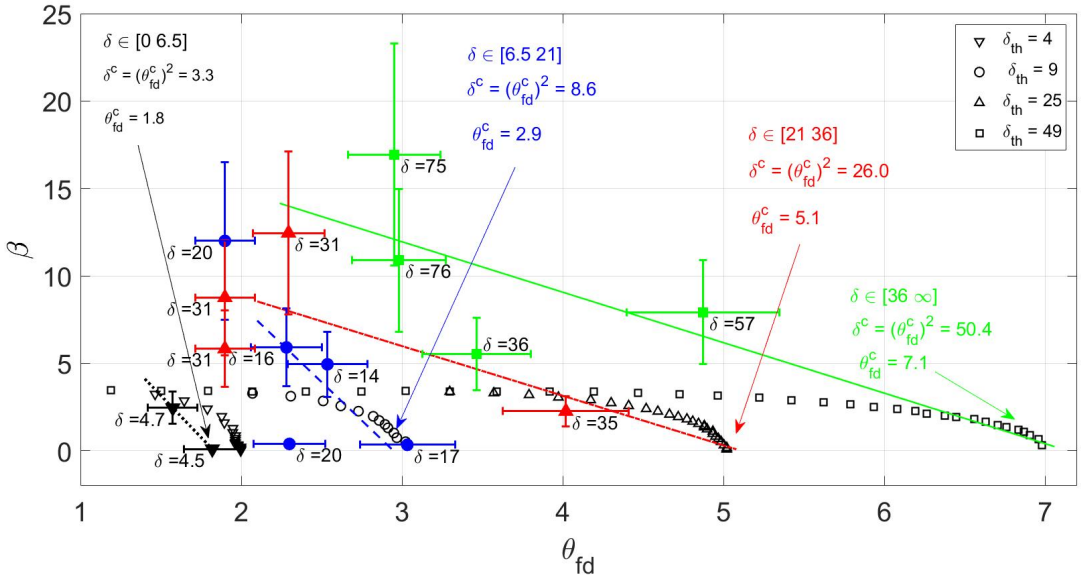

Figure 20: Same as figure (18), but we have added linear regression lines between β and θ_{fd}: Empty symbols: theoretical values for $\delta_{th} = 4$ (∇), $\delta_{th} = 9$ ($\circ$), $\delta_{th} = 25$ ($\triangle$), $\delta_{th} = 49$ ($\square$). Full symbols and regression lines: experimental values: dotted line and ($\blacktriangledown$) : $\delta \in [0\ \ 6.5]$, dashed line and ($\bullet$), $\delta \in [21\ \ 36]$ ($\blacktriangle$), $\delta \in [36\ \ \infty]$($\blacksquare$) : $\delta \in [36\ \ \infty]$. The critical experimental values of θ^c_{fd} and δ^c for which there is no amplification ($\beta = 0$) by bins of δ are written in the figure.

were relatively low to avoid wave breaking, aerodynamics effect of high steepnesses on the air-flow. Several studies have been conducted in the past on the effect of shallow water on drag coefficients and momentum transfers, but until this one, no specific work has been done on water tank experimental evidence of wave growth by the wind when the water depth is low without breaking events. Although still limited, the results derived from this unique wind wave tank experiment shed new light on the relationship between drag, U_{10}, friction velocity, roughness length, wave growth (γ-types or β-types), and other non-dimensional parameter (depth, energy, frequency)

We confirm that the dependence of C_d on wind speed is modified by water depth. Low depth increases Drag coefficient C_d, roughness length z_0, Charnock parameter α_{Ch}. This implies that for a given wind speed, momentum transfer from air to water is higher when the water depth is low.

All data are within the [Young, 1997; Young and Verhagen, 1996 a; Bretschneider, 1958] depth asymptotic limits. So, even if our measurements are not open field measurements, they follow well the natural limits observed in real open seas.

When the water depth is very low, the growth rate decreases zero amplification for some combinations of non-dimensional parameters $\delta = \frac{gh}{U_1^2} = \frac{gh\kappa^2}{u*^2}$ and $\theta_{fd} = \frac{\kappa}{u*}\sqrt{\frac{g}{k}\tanh kh}$. The non-dimensional water depth parameter δ depending on depth and on a characteristic wind speed, induces theoretically a family of curves representing the wave growth as a function of the wave phase velocity and the wind speed Montalvo et al. [2013 a,b]; Latifi et al. [2017]. Our experimental data follow those theoretical curves, with a decrease towards null amplification for some low depth values in conjugation with particular wind speeds. To date, no fully consistent and conclusive theory of wave amplification by wind exists. We are focused here on the Miles' mechanism, because we used quite low wind speed and low wave steepnesses conditions to avoid breaking and/or air flow separation that could be generated by steep waves, but probably the Miles' mechanism is not the only mechanism involved in the amplification of waves in finite depth conditions.

At the water surface the momentum transfer $\tau = \rho_a u*^2$ is split into two distinct parts: the form drag τ_{form}, and the viscous drag $\tau_{viscous}$ [Makin and Kudryavtsev, 2002; Donelan et al., 2012]: $\tau = \tau_{form} + \tau_{viscous}$. The form drag τ_{form} is the part of the momentum transfer that goes to the amplification of the waves, i.e. it induces directly the wave growth by the wind [Grare et al., 2013]. The form drag arises from the form of the waves and becomes higher as the steepness of the waves increases. The steeper the waves the greater the contribution of the wave drag to the total drag. The viscous drag $\tau_{viscous}$, also called surface tangential viscous stress or skin friction drag [Veron et al., 2007; Buckley et al., 2020], comes about through the direct molecular interaction at the interface. This viscous drag is the part of the momentum transfer that goes to the generation and amplification of the surface current, i.e. the surface drift. in this study, we have shown that, in low depth conditions, a) momentum flux τ increases and b) wave growth decreases, i.e. τ_{form} decreases. Then, by simple deduction from $\tau_{viscous} = \tau - \tau_{form}$, because τ increases and τ_{form} decreases, the viscous drag $\tau_{viscous}$ should increase significantly when the water depth is low.

From a theoretical point of view Miles theory in finite depth [Montalvo et al., 2013 a] was recently extended into the case with vorticity [Kern et al., 2021]. In the future, it would be interesting to conduct experiments in this wave tank to measure the influence of water depth on the surface wind drift current and water vorticity. This kind of experimental study, to our knowledge, has never previously been done. More data and analysis are needed to confirm these findings. Another point is that all the theories and developments on wave growth over finite depth involve water of constant depth, which is very restrictive. Even in the most ideal of field basins such a situation never exists. Variable depth effect on air-sea interactions is still an open issue.

Acknowledgements: H.B thanks IRPHE "appel d'offres interne" for the financial support of wind sensors. M.A.M. thanks the KIM Sea and Coast project for their funding.

Credit authorship contribution statement. H. Branger: experiments, software and data processing, original draft preparation, writing, editing, final manuscript. M.A. Manna: conceptualization, supervision, writing, editing, funding. C. Luneau: experiments. M. Abid: expertise, methodology, review. Ch. Kharif: supervision, investigation.

Data statements: Experimental data collected and analysed in this article can be obtained upon request from author Hubert Branger at `branger@irphe.univ-mrs.fr`

Conflicts of Interest: The authors declare no conflict of interest.

Appendix A. Relative errors

By making several times the same experiment, the relative precision on $(\bar{a_0})_{U_0}$, $(\bar{a_0})_{U_{ref}}$, $(\bar{a_1})_{U_0}$, and $(\bar{a_1})_{U_{ref}}$ was estimated to be 8%: $\frac{d\bar{a}}{\bar{a}} = 8\%$. The precision on $u*$ and on U_{10} is 15%, the precision on z_0 is 30%. $\frac{du*}{u*} = 15\%$, $\frac{dU_{10}}{U_{10}} = 15\%$, $\frac{dz_0}{z_0} = 30\%$. These error values may appear quite important but they are in the range values that can be found in literature for wave tank measurements [Zavadsky and Shemer, 2012].

Since $C_{d10} = (\frac{u*}{U_{10}})^2$, the relative precision on C_{d10} is: $\frac{dC_{d10}}{C_{d10}} = 2(\frac{du*}{u*} + \frac{dU_{10}}{U_{10}}) = 60\%$.

Since $\alpha_{Ch} = \frac{gz_0}{u*^2}$, the relative precision on α_{Ch} is : $\frac{d\alpha_{Ch}}{\alpha_{Ch}} = \frac{dz_0}{z_0} + 2\frac{du*}{u*} = 60\%$.

The precision on f_0 is 2%: $\frac{df_0}{f_0} = 2\%$. The precision on h is 1%: $\frac{dh}{h} = 1\%$, the precision on x is 0.5% : $\frac{dx}{x} = 0.5\%$.

Since $L_0 \approx \frac{g}{2\pi f_0^2}$, we have $\frac{dL_0}{L_0} = 2\frac{df_0}{f_0} = 4\%$.

The precision on non-dimensional depth is: $\frac{d(k_0 h)}{k_0 h} = \frac{dk_0}{k_0} + \frac{dh}{h} = \frac{dL_0}{L_0} + \frac{dh}{h} = 5\%$.

The precision on steepness is: $\frac{d(ak)_0}{(ak)_0} = \frac{da}{a} + \frac{dk_0}{k_0} = 12\%$.

The precision on celerity is: since $c_0 \approx \frac{g}{\omega}$, $\frac{dc_0}{c_0} = \frac{d\omega}{\omega} = \frac{df_0}{f_0} = 2\%$.

$C_{g0} = \frac{\mathrm{d}\omega}{\mathrm{d}k}$. We estimated the precision on C_{g0} as : $\frac{d(C_{g0})}{C_{g0}} \approx \frac{d\omega}{\omega} + \frac{dk}{k} = 6\%$.

The reference wind speed speed U_1 was taken as $U1 = u*/\kappa$ [Montalvo et al., 2013 a,b; Latifi et al., 2017].

$\delta = \frac{gh}{U_1^2} = \frac{gh\kappa^2}{u*^2}$, so $\frac{d\delta}{\delta} = \frac{dh}{h} + 2\frac{du*}{u*} = 1\% + 30\% = 31\%$.

$\theta_{dw} = \frac{1}{U_1}\sqrt{\frac{g}{k}} = \frac{\kappa}{u*}\sqrt{\frac{g}{k}}$, so $\frac{d\theta_{dw}}{\theta_{dw}} = \frac{du*}{u*} + \frac{1}{2}\frac{dk}{k} = 15\% + 2\% = 17\%$.

$\theta_{fd} = \theta_{dw}\sqrt{\tanh kh}$, so $\frac{d\theta_{fd}}{\theta_{fd}} \approx \frac{d\theta_{dw}}{\theta_{dw}} + \frac{1}{2}\frac{2kh}{sinh(2kh)}(\frac{dk}{k} + \frac{dh}{h}) < 17\% + \frac{1}{2}(4\% + 1\%) = 19.5\%$.

From equation (23) the precision on $\hat{\gamma}_{et}$ is:
$\frac{d\hat{\gamma}_{et}}{\hat{\gamma}_{et}} \approx \frac{du*}{u*} + \frac{d(C_{g0})}{C_{g0}} + 4\,\frac{d\bar{a}}{\bar{a}} + 2\,\frac{dx}{x} = 15\% + 6\% + 32\% + 1\% = 54\%.$

From equation (24) the precision on β is:
$\frac{d\beta}{\beta} \approx 2\,\frac{du*}{u*} + 2\,\frac{dc_0}{c_0} + \frac{d\omega}{\omega} + \frac{d(C_{g0})}{C_{g0}} + 4\,\frac{d\bar{a}}{\bar{a}} + 2\,\frac{dx}{x} = 30\% + 4\% + 2\% + 6\% + 32\% + 1\% = 75\%.$

From equation (25) the precision on γ_{et}/f_0 is:
$\frac{d(\gamma_{et}/f_0)}{\gamma_{et}/f_0} \approx \frac{d(C_{g0})}{C_{g0}} + \frac{df_0}{f_0} + 4\,\frac{d\bar{a}}{\bar{a}} + 2\,\frac{dx}{x} = 6\% + 2\% + 32\% + 1\% = 41\%.$

By making several times the same experiment, the relative precision on σ, the standard deviation of the water elevation, was found to be the same as the precision on the mean amplitude $\bar{a}$: $\frac{d\sigma}{\sigma} = \frac{d\bar{a}}{\bar{a}} = 8\%$.

The precision on U_{10}/c_0 is : $\frac{(dU_{10}/c_0)}{U_{10}/c_0} = \frac{dU_{10}}{U_{10}} + \frac{dc_0}{c_0} = 15\% + 2\% = 17\%$

The precision on gh/U_{10}^2 is : $\frac{d(gh/U_{10}^2)}{gh/U_{10}^2} = \frac{dh}{h} + 2\frac{dU_{10}}{U_{10}} = 1\% + 2(15)\% = 31\%$

The precision on $f_0 U_{10}/g$ is : $\frac{d(f_0 U_{10}/g)}{f_0 U_{10}/g} = \frac{df_0}{f_0} + \frac{dU_{10}}{U_{10}} = 2\% + 15\% = 17\%$

The precision on $g^2\,\sigma^2/U_{10}^4$ is : $\frac{d(g^2\sigma^2/U_{10}^4)}{g^2\sigma^2/U_{10}^4} = 2\frac{d\sigma}{\sigma} + 4\frac{dU_{10}}{U_{10}} = 2(8)\% + 4(15)\% = 76\%.$

References

Anctil, F., Donelan, M., 1986. Air water momentum flux observations over shoaling waves. Journ. Phys. Ocean. 26, 1344–1353.

Anderson, R., 1993. A study of wind stress and heat flux over the open ocean by the inertial-dissipation. Jour. Phys. Ocean. 23, 2153–2161.

Belcher, S.E., Harris, J.A., Street, R., 1994. Linear dynamics of wind waves in coupled turbulent air-water flow. part1 theory. Journ. Fluid Mech. 271, 119–151.

Belcher, S.E., Hunt, J.C.R., 1993. Turbulent shear flow over slowly moving waves. Journ. Fluid Mech. 251, 109–148.

Benjamin, B.T., Feir, J., 1967. The disintegration of wave trains on deep water. Journ. Fluid Mech. 27, 417–430.

Bi, X., Gao, Z., Liu, Y., Liu, F., Song, Q., Huang, J., Huang, H., Mao, W., Liu, C., 2015. Observed drag coefficients in high winds in the near offshore of the south china sea. Journ. Geoph. Res. Atmos. 120, 6444–6459.

Bliven, L.F., Huang, N., Long, S., 1986. Experimental study of the influence of wind on benjamin-feir sideband instability. Journ. Fluid Mech. 162, 237–260.

Bretschneider, C.L., 1954. Generation of wind waves over a shallow bottom. Beach erosion board 51, 24.

Bretschneider, C.L., 1958. Revised wave forecasting relationships. In: Proc. 6th Conference on Coastal Engineering, Gainsville/Palm Beach/Miami Beach, ASCE, New York, FL. ASCE, New York, 30–67.

Bruch, W., Piazzola, J., Branger, H., van Eijk, A., Luneau, C., Bourras, D., Tedeschi, G., 2021. Sea-spray-generation dependence on wind and wave combinations: A laboratory study. Bound. Lay. Met. 180, 477–505.

Buckley, M., Veron, F., Yousefi, K., 2020. Surface viscous stress over wind-driven waves with intermittent airflow separation. Journ. Fluid Mech. 905, A31.

CERC, 1977. Shore protection manual. U.S. Army Coastal Engineering Research Center. 3 Volumes.

CERC, 1984. Shore protection manual. U.S. Army Coastal Engineering Research Center. 2 Volumes.

Charnock, H., 1955. Wind stress on a water surface. Quart. Journ. Roy. Meteorol. Soc. 81, 639–640.

Chen, S., Qiao, F., Jiang, W., Guo, J., Dai, D., 2019. Impact of surface waves on wind stress under low to moderate wind conditions. Journ. Phys. Ocean. 49, 2017–2028.

Coantic, M., Ramamonjiarisoa, A., Mestayer, P., Resch, F., Favre, A., 1981. Wind-water tunnel simulation of smallscale ocean–atmosphere interactions. Journ. Geoph. Res. Ocean. 86, 6607–6626.

Conte, S.D., Miles, J.W., 1959. On the numerical integration of the orr-sommerfeld equation. Journal of Society of industrial and applied mathematics 7, 361–366.

Deardorff, J., 1967. Aerodynamic theory of wave growth with constant wave steepness. Journ. Oceanol. Soc. Jpn. 23, 278–297.

Donelan, M., Curcic, M., Chen, S., A.K., M., 2012. Modeling waves and wind stress. Journ. Geoph. Res. Ocean. 117, C00J23.

Donelan, M.A., 1982. The dependence of the aerodynamic drag coefficient on wave parameters. Amer. Meteor. Soc., The Hague, Netherlands , 381–387.

Donelan, M.A., Babanin, A.V., Young, I.R., Banner, M.L., 2006. Wave-follower field measurements of the wind-input spectral function. part 2 : Parameterization of the wind input. Journ. Phys. Ocean. 36, 1672–1689.

Donelan, M.A., Babanin, A.V., Young, I.R., Banner, M.L., McCormick, C., 2005. Wave-follower field measurements of the wind-input spectral function. part 1 : Measurements and calibrations. Journ. Atmos. Ocean. Tech. 22, 799–813.

Donelan, M.A., Skafel, M., Graber, H., Liu, P., Schwab, D., Venkatesh, S., 1992. On the growth rate of wind-generating waves. Atmos.-Ocean 30, 457–478.

Drazin, P.G., Reid, W., 1982. Hydrodynamic Stability. Cambridge University Press.

Gao, Z., Wang, Q., Zhou, M., 2009. Wave-dependence of friction velocity, roughness length, and drag coefficient over coastal and openwater surfaces by using three databases. Adv. Atm. Sci. 26, 887–894.

Garratt, J.R., 1977. Review of drag coefficients over oceans and continents. Mon. Weather Rev. 105, 915–929.

Gaster, M., 1962. A note on the relation between temporally-increasing and spatially-increasing disturbances in hydrodynamic stability. Journ. Fluid Mech. 14, 222–224.

Geernaert, G., 1987. Measurements of the wind stress, heat flux, and turbulence intensity during storm conditions over the north sea. Journ. Geop. Res. 92, 13127–13130.

Geernaert, G., Katsaros, K., K., R., 1986. Variation of the drag coefficient and its dependance on sea state. Journ. Geop. Res. Ocean. 91, 7667–7679.

Grare, L., Peirson, W., Branger, H., Walker, J., Giovanangeli, J., Makin, V., 2013. Growth and dissipation of wind-forced, deep-water waves. Journ. Fluid Mech. 722, 5–50.

Hsu, H.C., Kharif, C., Abid, M., Chen, Y., 2018. A nonlinear schrodinger equation for gravity - capillary water waves on arbitrary depth with constant vorticity. part 1. Journ. Fluid Mech. 854, 146–163.

Hwung, H., Chiang, W., Yang, R., I.V., S., 2011. Threshold model on the evolution of stokes wave side-band instability. Europ. Journ. Mech. B/Fluids 30, 147–155.

Iafrati, L.F., Babanin, A., Onorato, M., 2014. Modeling of ocean atmosphere interaction phenomena during the breaking of modulated wave trains. Journ. Comput. Phys. 271, 151–171.

Ijima, T., Tang, F., 1966. Numerical calculations of wind waves in shallow water. Proc. 10th Conf. on Coastal Eng., Tokyo. ASCE, New York. 2, 38–45.

Janssen, P.A.E.M., 2004. The interaction of ocean waves and wind. Cambridge University Press.

Jeffreys, H., 1924. On the formation of waves by wind part1. Proc. Royal Soc. London. Series A: Math. and Phys. Sci. A107, 189–206.

Jeffreys, H., 1925. On the formation of waves by wind part2. Proc. Royal Soc. London. Series A: Math. and Phys. Sci. A110, 341–347.

Jimenez, P., Dudhia, J., 2018. On the need to modify the sea surface roughnessformulation over shallow waters. Journ. Appl. Meteo. and Clim. 57, 1101–1110.

Kabardin, I., Meledin, V., Dvoinishnikov, S., Troitskaya, Y., Kandaurov, A., Sergeev, D., 2020. Approbation of the laser doppler anemometer under kinematic flow parameters diagnostics during spray formation in a laboratory wind-wave interaction modelling. Journal of Physics. 1675, IOP publishing, 180–191.

Kern, N., Chaubet, C., Kraenkel, R., Manna, M.A., 2021. Miles' mechanism for generating surface water waves by wind, in finite water depth and subject to constant vorticity flow. Coastal Eng. 170, 103976.

Kitaigorodskii, S., 1970. The physics of air-sea interaction, English Edition 1973. Israel Prog. for Sci. trans., P. Greenberg Editor.

Kitaigorodskii, S., Volkov, Y., 1965. On the roughness parameter of the sea surface and the calculation of momentum flux in the near water layer of the atmosphere. Izv. Atmos. Ocean Phys. 1, 973–988.

Komen, G., 1994. Sea surface winds and atmospheric circulation. Cambridge Univ. Press, M. Donelan, K. Hasselmann, S. Hasselmann, and P. A. E. M. Janssen Eds.

Kozlova, D., Troitskaya, Y., 2021. On the role of the explosive interaction of three surface waves at the initial stage of spray generation in strong winds. Atmospheric and Oceanic Physics. 57, 180–191.

Larson, T.R., Wright, J.W., 1975. Wind-generated gravity-capillary waves: Laboratory masurements of temporal growth rates using microwave backscatter. Journ. Fluid Mech. 70, 417–436.

Latifi, A., Manna, M.A., Montalvo, P., Ruivo, M., 2017. Linear and weakly nonlinear models of wind generated surface waves in finite depth. Journ. App. Fluid Mech. 10, 1829–1843.

Lüko, G., Torma, P., Krámer, T., Weidinger, T., Vecenaj, Z., Grisogono, B., 2020. Observation of wave-driven air–water turbulent momentum exchange in a large but fetch-limited shallow lake. Adv. Sci. Res. 17, 175–182.

Longo, S., 2012. Wind-generated water waves in a wind tunnel: Free surface statistics, wind friction and mean air flow properties. Coastal Eng. 61, 27–41.

MacMahan, J., 2017. Increased aerodynamic roughness owing to surfzone foam. Journ. Phys. Ocean. 47, 2115–2122.

Makin, V., Caulliez, G., Kudryavtsev, V., 2004. Drag of the water surface at limited fetch: laboratory measurements and modelling. Geoph. Res. Abstracts. 6, EGU04–A–00113.

Makin, V., Kudryavtsev, V., 2002. Impact of dominant waves on s ea drag. Bound. Lay. Met. 103, 83–99.

Miles, J.W., 1957. On the generation of surface waves by shear flows. Journ. Fluid Mech. 3, 185–204.

Miles, W., 1967. Surface-wave damping in closed basins. Proc. Royal Soc. London. Series A: A297, 459–473.

Monin, A., Obukhov, A., 1954. Basic laws of turbulent mixing in the surface layer of the atmosphere. Tr. Akad. Nauk SSSR Geophiz. Inst. 24, 163–187.

Montalvo, P., Dorignac, J., Manna, M.A., Kharif, C., Branger, H., 2013 a. Growth of surface wind-waves in water of finite depth. a theoretical approach. Coastal Eng. 77, 49–56.

Montalvo, P., Kraenkel, R., Manna, M., Kharif, C., 2013 b. Wind-wave amplification mechanisms: possible models for steep wave events in finite depth. Natural Hazards and Earth System Sciences. 13, 2805–2813.

Oost, W., Komen, G., Jacobs, C., Vanoort, C., 2002. New evidence for a relation between wind stress and wave age from measurements during asgamage. Bound. Lay. Met. 103, 409–438.

Ortiz-Suslow, D.G., Haus, B.K., Williams, N.J., Graber, H.C., MacMahan, J.H., 2018. Observations of air-sea momentum flux variability across the inner shelf. Journ. Geoph. Res. Oceans. 123, 8970–8993.

Perlin, M., Choi, W., Tian, Z., 2013. Breaking waves in deep and intermediate waters. Annual Review of Fluid Mech. 45, 115–145.

Phillips, O., 1957. On the generation of waves by turbulent wind. Journ. Fluid Mech. 2, 417–445.

Plant, W., 1982. A relationship between wind stress and wave slope. Journ. of Geoph. Res. 87, 1961–1967.

Rayleigh, L., 1880. On the stability, or instability, of certain fluid motions. Proc. Lond. Math. Soc XI, 57–70.

Shabani, B., Nielsen, P., Baldock, T., 2014. Direct measurements of wind stress over the surf zone. Journ. Geophys. Res. Oceans 119, 2949–2973.

Shemdin, O.H., Hsu, E.Y., 1967. Direct measurement of aerodynamic pressure above a simple progressive gravity wave. Journ. Fluid Mech. 30, 403–416.

Shemer, L., Singh, S., 2021. Spatially evolving regular water wave under the action of steady wind forcing. Phys. Rev. Fluids 6, 034802.

Smith, S., 1980. Wind stress and heat flux over the ocean in gale force winds. Journ. Phys. Ocean. 10, 709–726.

Smith, S., Anderson, R., Oost, W., Kraan, C., Maat, J., DeCosmo, J., Katsaros, B., Davidson, K., Bumke, K., Hasse, L., H.M., C., 1992. Sea surface wind stress and drag coefficients: the hexos results. Bound. Lay. Met. 60, 109–142.

Snyder, R.L., Dobson, F.W., Elliot, J.A., Long, R.B., 1981. Array measurements of atmospheric pressure fluctuations above surface gravity waves. Journ. Fluid Mech. 102, 1–59.

Sverdrup, H.V., Munk, W., 1947. Wind, sea and swell: theorie of relation for forecasting. Hydrdrographyc office, US Navy 601.

Thijsse, J., 1949. Dimensions of wind-generated waves. General Assembly of Association d'Océanographie Physique, Oslo. Procés-Verbaux. 4, 80–81.

Toffoli, A., Loffredo, L., LeRoy, P., Lefèvre, J., Babanin, A., 2012. On the variability of sea drag in finite water depth. Journ. Geoph. Res. Oceans 117, C00J25.

Troitskaya, Y., Druzhinin, O., Ser v, D., Kandaurov, A., Ermakova, O., Tsai, W., 2018. Quasi-linear approximation for description of turbulent boundary layer and wind wave growth. Procedia IUTAM, IUTAM symposium on wind waves. 26, 194–203.

Van Dorn, W., 1966. Boundary dissipation of oscillatory waves. Journ. Fluid Mech. 24, 769–779.

Veron, F., 2015. Ocean spray. Annual Review of Fluid Mechanics 47, 507–538.

Veron, F., Saxena, G., Misra, S., 2007. Measurements of the viscous tangential stress in the airflow above wind waves. Geophys. Res. Lett. 34, L19603.

Vickers, D., Mahrt, L., 1997. Fetch limited drag coefficients. Bound. Layer Met. 85, https://doi.org/10.1023/A:1000472623187.

Villefer, A. and. Benoit, M., Violeau, D., Luneau, C., Branger, H., 2021. Influence of following, regular and irregular long waves on wind-wave growth with fetch: an experimental study. Journ. Phys. Oceanogr. 55, 3435–3448.

Wu, H.Y., Hsu, E.Y., Street, R.L., 1977. The energy transfer due to air-input, non-linear wave-wave interaction and white-cap dissipation associated with wind-generated waves. Tech. Rep. Stanford Univ. 207, 1–158.

Wu, H.Y., Hsu, E.Y., Street, R.L., 1979. Experimental study of nonlinear wave-wave interaction and white-cap dissipation of wind-generated waves. Dyn. Atmos. Oceans. 3, 55–78.

Wu, J., 1980. Wind stress coefficient over sea surface near neutral conditions. Journ. Phys. Ocean. 10, 727–740.

Wu, J., 1982. Wind-stress coefficients over sea surface from breeze to hurricane. Journ. Geoph. Res. 87, 9704–9706.

Yelland, M.J., Moat, B.I., Taylor, P.K., Pascal, R., Hutchings, J., Cornell, V., 1998. Wind stress measurement of the open ocean drag coefficient corrected for air flow disturbance by the ship. Journ. Phys. Ocean. 28, 1511–1526.

Young, I.R., 1997. The growth rate of finite depth wind-generated waves. Coastal Eng. 32, 181–195.

Young, I.R., 1999. Wind Generated Ocean Waves. volume 2. Elsevier Ocean Engineering Book Series.

Young, I.R., Banner, M., Donelan, M., Babanin, A., Melville, W., Veron, F., mcCormick, C., 2005. An integrated system for the study of wind wave source terms in finite depth water. Journ. Atmos. Oceanic Technol. 22, 814–828.

Young, I.R., Verhagen, L.A., 1996 a. The growth of fetch limited waves in water of finite depth. part i : Total energy and peak frequency. Coastal Eng. 29, 47–78.

Young, I.R., Verhagen, L.A., 1996 b. The growth of fetch limited waves in water of finite depth. part ii : Spectral evolution. Coastal Eng. 29, 79–99.

Yousefi K., V.F., M.P, B., 2021a. 'momentum flux measurements in the airflow over wind-generated surface waves. Journ. Fluid Mech. 895, A15.

Yousefi K., V.F., M.P, B., 2021b. Turbulent and wave kinetic energy budgets in the airflow over wind-generated surface waves. Journ. Fluid Mech. 920, A33.

Zavadsky, A., Shemer, L., 2012. Characterization of turbulent airflow over evolving water-waves in a wind-wave tank. Journ. of Geoph. Res. 117, 1961–1967.

Zhao, W., Liu, Z., Dai, C., Song, G., Lv, Q., 2015. Typhoon air-sea drag coefficient in coastal regions. Journ. Geoph. Res. Ocean. 120, 716–727.